ORIGINAL PAPER



Four-dimensional thermal evolution of the East African Orogen: accessory phase petrochronology of crustal profiles through the Tanzanian Craton and Mozambique Belt, northeastern Tanzania

Francisco E. Apen^{1,2} · Roberta L. Rudnick^{1,2} · John M. Cottle^{1,2} · Andrew R. C. Kylander-Clark^{1,2} · Madalyn S. Blondes³ · Philip M. Piccoli⁴ · Gareth Seward¹

Received: 20 March 2020 / Accepted: 18 September 2020 © Springer-Verlag GmbH Germany, part of Springer Nature 2020

Abstract

U–Pb petrochronology of deep crustal xenoliths and outcrops across northeastern Tanzania track the thermal evolution of the Mozambique Belt and Tanzanian Craton following the Neoproterozoic East African Orogeny (EAO) and subsequent Neogene rifting. At the craton margin, the upper–middle crust record thermal quiescence since the Archean (2.8–2.5 Ga zircon, rutile, and apatite in granite and amphibolite xenoliths). The lower crust of the craton documents thermal pulses associated with Neoarchean ultra-high temperature metamorphism (ca. 2.64 Ga, > 900 °C zircon), the EAO (600–500 Ma rutile), and fluid influx during rifting (< 5 Ma apatite). Rutile in garnet granulite xenoliths exhibits partial Pb loss related to slow cooling of the lower crust after the EAO and suggests residence at 500–600 °C prior to entrainment. In contrast to the craton, the entire crust of the Mozambique Belt underwent differential cooling following the EAO. Both the upper and middle crust record metamorphism from 640 to 560 Ma (zircon, monazite, and titanite) and rapid exhumation at 510–440 Ma (rutile and apatite). Lower crustal xenoliths contain Archean zircon, but near-zero age rutile and apatite, indicating residence > 650 °C (above Pb closure of rutile and apatite) at the time of eruption. Zoned titanite records growth during cooling of the lower crust at 550 Ma, followed by fluid influx during slow cooling and exhumation (0.1–1 °C/Myr after 450 Ma). Permissible lower-crustal temperatures for the craton and orogen suggest variable mantle heat flow through the crust and reflect differences in mantle lithosphere thickness rather than advective heating from rifting.

Keywords Xenoliths · Lower crust · East African orogen · Petrochronology · Collisional orogen

Communicated by Othmar Müntener.

Electronic supplementary material The online version of this article (https://doi.org/10.1007/s00410-020-01737-6) contains supplementary material, which is available to authorized users.

- Francisco E. Apen apen@ucsb.edu
- Department of Earth Science, University of California, Santa Barbara, CA 93106-9630, USA
- Earth Research Institute, University of California, Santa Barbara, CA 93106-9630, USA
- ³ U. S. Geological Survey, Reston, VA 20192, USA
- Department of Geology, University of Maryland, College Park, MD 20742, USA

Published online: 09 October 2020

Introduction

As samples of in situ deep crust, xenoliths carried rapidly to the surface by alkali basalts and kimberlites yield unique insights into lithosphere formation and evolution. They can provide direct constraints on the long-term thermal evolution and structure of the lithosphere, which in turn bear on models of heat transfer between the crust and mantle, the thermal evolution of orogens, the distribution of heat-producing elements in the crust, and the bulk composition of continental crust (Pollack and Chapman 1977; Rudnick et al. 1998; Jaupart and Mareschal 2014).

Integrating data from multiple geochronometers and thermochronometers in xenoliths enables reconstructions of the thermal histories of continental crust. The U–Pb systematics of phases with different Pb closure temperatures—zircon,

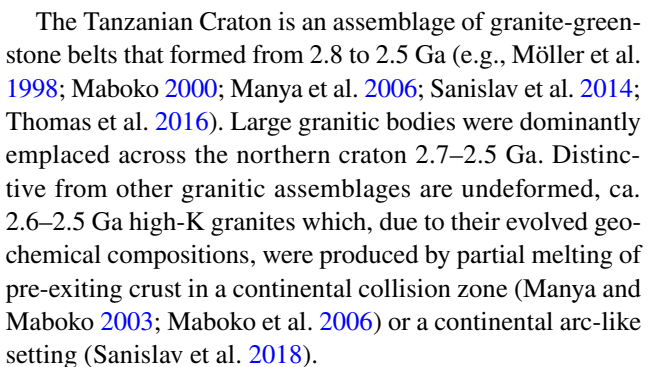


titanite, rutile, and apatite—commonly found in crustal lithologies provide constraints on the timing, duration, and rate of deep crustal heating and cooling (e.g., Davis 1997; Davis et al. 2003; Schmitz and Bowring 2003a, b; Blackburn et al. 2011). This is because the length scales of U–Pb zonation in each of these minerals varies with the intensity and duration of thermal events, with length scales increasing with greater intensities and/or longer durations of heating (e.g., Dodson 1986; Kooijman et al. 2010; Blackburn et al. 2011; Smye et al. 2018). Thermal histories extracted from U-Pb data can be further tested and refined when they are combined with trace element data from the same phases—the length scales of trace elements should also vary with the extent of heating and cooling. Trace-element data can also provide complementary information on thermal histories, such as crystallization temperatures or evidence for equilibration with major phases like garnet (e.g., Zack et al. 2004; Ferry and Watson 2007; Hayden et al. 2008). Critically, multiaccessory phase U-Pb and trace element data are able to document long-term thermal histories that may be otherwise overlooked by conventional major-element exchange thermobarometry, especially in dry, lower crustal lithologies (e.g., Spencer et al. 2013; Garber et al. 2017).

Here we report in situ petrochronology data for crustal xenoliths erupted in young rift basalts (< 1 Ma) on the Archean Tanzanian Craton and adjacent Proterozoic Mozambique Belt in northeastern Tanzania, and outcrop samples from the Mozambique Belt. The xenoliths derive from variable crustal depths and, together with the outcrops, form composite sections through the crust. Coupled U-Pb and trace element laser ablation zircon, monazite, titanite, rutile, and apatite data from these sections afford a rare opportunity to assess how the crust has evolved in an area with a complex tectonic history. In northeast Tanzania, key geologic events include crust formation and metamorphism in the Archean, continental collision during the Neoproterozoic East African Orogeny, and present-day rifting. We use our data to address how orogeny and recent rifting affected the long-term thermal state of the deep crust and to document lateral variations in the present-day thermal structure of the crust.

Geologic setting

Northeastern Tanzania is composed of the Archean Tanzanian Craton and the Mozambique Belt (Fig. 1) (Stern 1994; Fritz et al. 2009). The latter consists of Archean–Mesoproterozoic crust that was metamorphosed to high grades during the Himalayan-scale Neoproterozoic East African Orogeny (e.g., Fritz et al. 2013) and is presently undergoing rifting. Each of these geological distinct regions and events are described below.



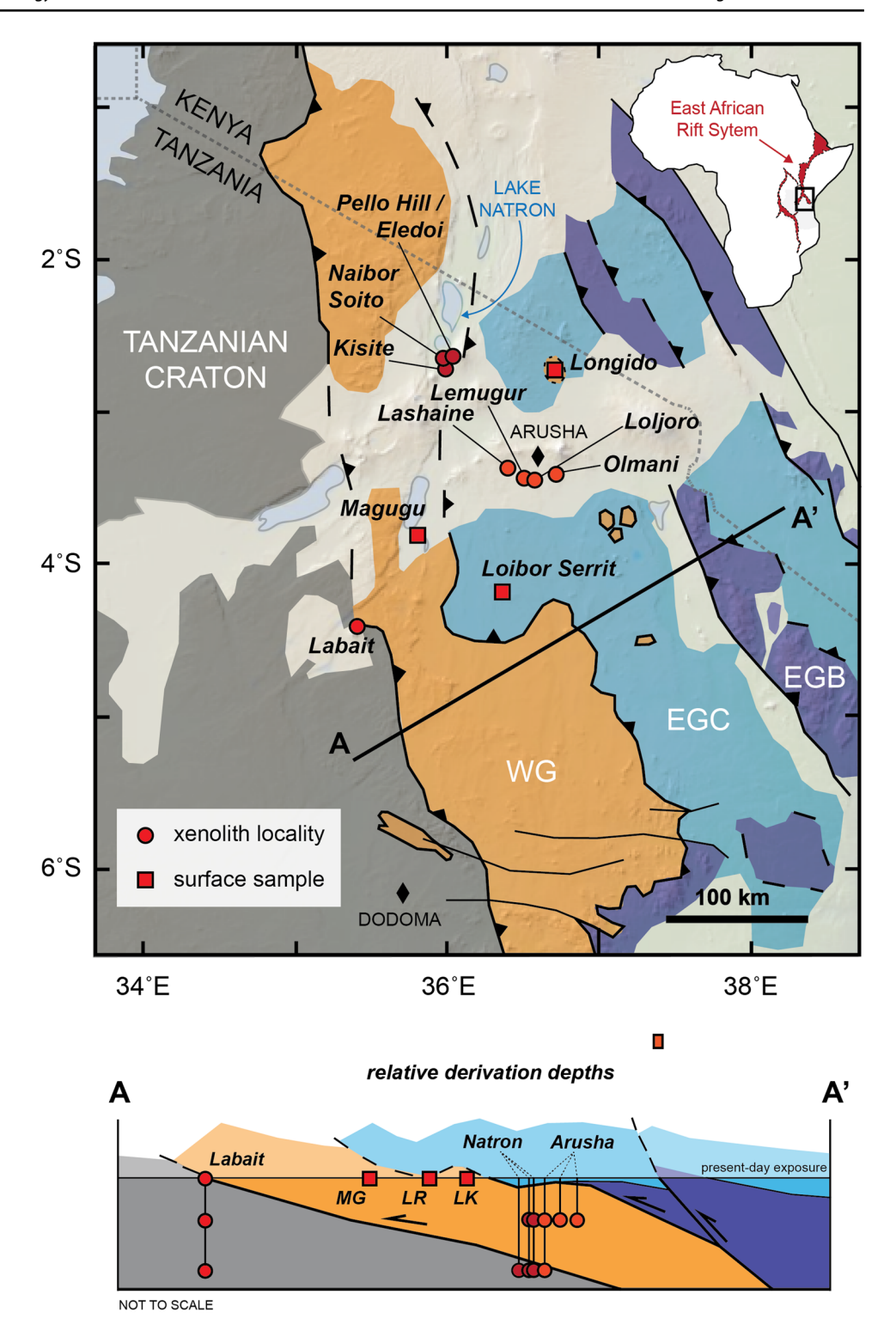
Both seismic (Ritsema et al. 1998; Weeraratne et al. 2003) and xenolith studies (Lee and Rudnick 1999; Chesley et al. 1999; Burton et al. 2000) suggest that the craton is underlain by a relatively thick (≥ 150 km), refractory, and Archean lithospheric mantle keel. Rayleigh wave tomography also reveals the presence of a thermal anomaly beneath the craton, which some have interpreted as evidence for a plume (e.g., Ritsema et al. 1998; Weeraratne et al. 2003). Indeed, mantle xenoliths from the deepest lithosphere bear evidence of heating and metasomatism (Lee and Rudnick 1999; Chesley et al. 1999; Aulbach et al. 2008) consistent with the influence of a plume. Yet, surface heat flow on the craton margin is generally low (average of 38 mW/m²; Nyblade et al. 1990; Nyblade 1997), suggesting that any thermal perturbation below or within the mantle lithosphere is not yet manifested at the surface (Nyblade and Brazier 2002; Weeraratne et al. 2003; Julià et al. 2005).

East of the Tanzanian Craton is the Mozambique Belt (Fig. 1), a polymetamorphic belt that underwent metamorphism during the Usagaran (ca. 2.0–1.8 Ga) and East African (ca. 640–560 Ma) orogenies (Fritz et al. 2013). Rocks recording the Usagaran orogeny crop out along the southeastern margin of the Tanzania Craton, but are absent in northern Tanzania. Instead, the Mozambique Belt in north Tanzania was dominantly metamorphosed during the East African Orogen (Stern 1994; Fritz et al. 2013). Here the belt is divided into the Western Granulites and the Eastern Granulites. Both are lithologically similar and extensively deformed, but they can be distinguished based on their metamorphic ages, metamorphic P-T paths, and protolith ages (Maboko 1997, 2001; Appel et al. 1998; Möller et al. 1998, 2000; Maboko and Nakamura 2002; Johnson et al. 2003; Sommer et al. 2003, 2005; Fritz et al. 2005, 2009; Tenczer et al. 2013).

The Eastern Granulites are divided into a basement and cover. The basement consists of mafic–felsic orthogneisses, anorthosites, and rarer metasedimentary units that are found primarily as uplifted blocks in the eastern portion of the East African Orogen (Fig. 1) (Appel et al. 1998; Fritz et al. 2005; Tenczer et al. 2006, 2013). The cover consists of granitic orthogneisses, marbles, and metapelitic lithologies that occupy the lowlands (Fig. 1) (Tenczer et al. 2006, 2013).



Fig. 1 Top: Simplified geologic map of northern Tanzania with sample locations. Areas in light gray are Quaternary-Tertiary volcanic and sedimentary cover. Red areas in inset represent the East African Rift system. Modified from Fritz et al. (2009). Background topography is from GeoMapApp. Bottom: Schematic cross-section along A-A' transect with inferred xenolith derivation depths projected (see text for details). WG Western Granulites, EGC Eastern Granulite cover, EGB Eastern Granulite basement, LB Labait, MG Magugu, LR Loibor Serrit, LK Longido, KS Kisite, LS Lashaine, PH Pello Hill, EL Eledoi, NS Naibor Soito, LG Lemugur, LJ Loljoro, OL Olmani



Whole-rock Sm–Nd model ages and zircon core U–Pb ages from the basement and cover are Meso- to Neoproterozoic (1500–700 Ma; Möller et al. 1998; Sommer et al. 2005; Hauzenberger et al. 2007; Tenczer et al. 2006, 201; Mtabazi et al. 2019). The Proterozoic dates overlap in age with arc rocks distributed from the Arabian–Nubian Shield to

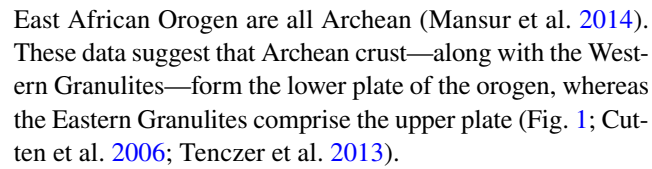
Madagascar (e.g., Fritz et al. 2013 and references therein) suggesting that the magmatic protoliths of the Eastern Granulites also formed in an arc outboard of Africa (e.g., Möller et al. 1998; Maboko and Nakamura 2002; Mole et al. 2018). Detailed petrologic and thermobarometric studies of the basement and cover consistently show counter-clockwise



P-T paths that attained peak metamorphism at 0.9-1.1 GPa and 750-850 °C, followed by near isobaric cooling at 0.8-1.0 GPa before undergoing final exhumation (Coolen et al. 1982; Muhongo and Tuisku 1996; Appel et al. 1998; Muhongo et al. 1999). These P-T paths have been interpreted to reflect metamorphism by magmatic underplating and loading at the base of a continental margin—as opposed to crustal thickening alone (e.g., Bohlen and Mezger 1989; Appel et al. 1998). Metamorphic monazite and zircon rims in rocks from the Eastern Granulites yield ca. 640-610 Ma dates (Möller et al. 1998, 2000; Tenczer et al. 2006, 2013; Thomas et al. 2016) and are associated with episodes of underplating/loading during arc assembly (Möller et al. 2000; Cutten et al. 2006; Tenczer et al. 2006). Multi-fraction titanite and rutile U-Pb thermal ionization mass spectrometry (TIMS) dates from the Eastern Granulite basement range from 620 to 610 Ma and 550 to 500 Ma, respectively, and have been interpreted to date isobaric cooling (Möller et al. 2000).

In contrast to the Eastern Granulites, the Western Granulites consist of Archean-age protoliths metamorphosed at amphibolite-granulite facies (e.g., Tenczer et al. 2013). Garnet-bearing orthogneisses and metapelites have polymetamorphic mineral assemblages that record metamorphism along clockwise P-T paths; peak metamorphism at 1.2-1.4 GPa and 700–850 °C was followed by isothermal decompression (Sommer et al. 2003, 2008; Johnson et al. 2003; Fritz et al. 2005; Cutten et al. 2006). Whole-rock Sm-Nd model ages and zircon and monazite U-Pb core dates range from 2.7 to 2.5 Ga (Möller et al. 1998; Johnson et al. 2003; Tenczer et al. 2013; Thomas et al. 2016). Metamorphic zircon and monazite rims are ca. 560-540 Ma and indicate that the Western Granulites protoliths were metamorphosed later than the Eastern Granulites (Johnson et al. 2003; Sommer et al. 2003; Cutten et al. 2006; Tenczer et al. 2013), though older ca. 640-610 Ma metamorphic zircon dates from some Western Granulite rocks have also been reported (e.g., Cutten et al. 2006; Le Goff et al. 2010). Along with petrologic evidence of isothermal decompression following peak metamorphism, 560-540 Ma dates have been interpreted as the timing of collision and exhumation during the amalgamation of Gondwana (Sommer et al. 2003, 2008; Johnson et al. 2003; Cutten et al. 2006). Whereas others distinguish this ca. 560-540 Ma period as the Kuunga Orogeny (e.g., Meert 1995, 2003), we refer to the entire span of Neoproterozoic events as the EAO.

The broad structure of the East African Orogen has been inferred from geophysical and xenolith studies. The crust of the orogen is estimated to be 38- to 42 km-thick based on S-wave receiver functions (Julià et al. 2005), but thermobarometry of lower crustal xenolith indicates that the crust was at least 60 km-thick during the EAO (Mansur et al. 2014). Zircon U–Pb dates of lower crustal xenoliths in the



Rayleigh wave tomography indicates that the mantle lithosphere beneath the orogen is thinner compared to the craton, but there are significant uncertainties in lithosphere thickness based on this method (Weeraratne et al. 2003). Thermobarometry on garnet-bearing peridotite xenoliths from Lashaine suggest a minimum thickness of ~165 km (Rudnick et al. 1994), though garnet-bearing mantle xenoliths are rare elsewhere in the orogen (Cohen et al. 1984; Dawson and Smith 1988; Aulbach et al. 2011). Compared to the craton, surface heat flow in the orogen is higher and more variable (40–60 mW/m², average 47 mW/m²; Nyblade 1997).

The East African rift system initiated in Ethiopia at ca. 40–30 Ma and propagated southward, reaching northern Tanzania by ca. 8 Ma (Ebinger 1989; Dawson 1992; Foster et al. 1997). Where the rift impinges against the Tanzanian Craton, it widens and diverges into a western and eastern branch (inset in Fig. 1). The western branch forms a series of segmented normal faults (e.g., Ebinger 1989), whereas the eastern branch is more magmatically active and forms numerous rift valleys that lie along older structures between the craton and orogenic belt and along sutures within the orogen (Dawson 1992; Nyblade and Brazier 2002; Le Gall et al. 2004, 2008). From 4.5 Ma to < 0.5 Ma, rifting along the eastern branch led to the eruption of numerous tuff cones (Dawson 1992; Le Gall et al. 2008), some of which bear xenoliths.

Samples

The xenoliths investigated in this study come from young (<1 Ma) rift basalts erupted on the Tanzanian Craton and Mozambique Belt (Fig. 1). Most of these localities carry mantle xenoliths in addition to crustal xenoliths. Mantle lithologies—garnet and spinel peridotites, pyroxenites, dunites, and glimmerites—have been widely investigated for their petrology, geochemistry, and physical properties (e.g., Dawson et al. 1970; Dawson and Smith 1988, 1992; Dawson 2002; Rudnick et al. 1993, 1994; Canil et al. 1994; Lee and Rudnick 1999; Chesley et al. 1999; Burton et al. 2000; Vauchez et al. 2005; Aulbach et al. 2011; Chin 2018; Xu et al. 2019), whereas previous work on crustal xenoliths is more limited (Dawson et al. 1970; Jones et al. 1983; Cohen et al. 1984; Bellucci et al. 2011; Mansur et al. 2014).

We have analyzed 32 crustal xenoliths and seven surface samples using laser-ablation split-stream inductively coupled plasma mass spectrometry (LASS) U–Pb and trace element petrochronology (Table 1). The xenoliths come from



 Table 1
 Sample descriptions

Sample locations and names	Rock type	Major phases	Accessory phases	Present-day crustal level
Tanzanian Craton				
Labait (4°34′02″S, 35°25′53	3"E)			
LB04-86	Granite	Pl + Qtz + Kfs + Ms + Chl	Zrn+Ap	Upper crust
LB04-05	Schist	Pl + Qtz + Kfs + Bt + Ms	Zrn+Ap	Middle crust
LB04-89	Amphibolite	Pl + Qtz + Hbl + Ep + Bt	Zrn + Rtl + Ap	Middle crust
LB04-92	Amphibolite	Pl + Qtz + Hbl + Bt	Zrn+Ap	Middle crust
LB04-36	Two-pyroxene granulite	Pl + Qtz + Cpx + Opx	$\mathbf{Zrn} + \mathbf{Ap} + \mathbf{Ilm}$	Lower crust
LB04-19	Two-pyroxene granulite	Pl + Kfs + Cpx + Opx	$\mathbf{Zrn} + \mathbf{Ap} + \mathbf{Ilm}$	Lower crust
LB04-82	Two-pyroxene granulite	Pl + Qtz + Kfs + Cpx + Opx + Bt	$\mathbf{Zrn} + \mathbf{Ap} + \mathbf{Ilm}$	Lower crust
LB04-91	Garnet orthopyroxene granulite	Grt + Pl + Qtz + Kfs + Opx	$\mathbf{Zrn} + \mathbf{Rtl} + \mathbf{Ap}$	Lower crust
LB04-39	Garnet orthopyroxene granulite	Grt + Pl + Qtz + Opx	$\mathbf{Zrn} + \mathbf{Rtl} + \mathbf{Ap}$	Lower crust
LB04-74	Garnet orthopyroxene granulite	Grt + Pl + Qtz + Kfs + Opx	Zrn+Rtl	Lower crust
Natron area				
Naibor Soito (2°46′53″S, 36	5°00′50″E)			
NS04-96	Two-pyroxene granulite	Pl + Qtz + Cpx + Opx	$\mathbf{Zrn} + \mathbf{Ap} + \mathbf{Ilm}$	Lower crust
NS04-150	Two-pyroxene granulite	Pl + Cpx + Opx + Hbl + Bt	$\mathbf{Zrn} + \mathbf{Ap} + \mathbf{Ilm}$	Lower crust
NS04-60	Garnet two-pyroxene granulite	Grt + Pl + Cpx + Opx + Hbl + Bt	$\mathbf{Zrn} + \mathbf{Rtl} + \mathbf{Ap} + \mathbf{Ilm}$	Lower crust
NS04-01	Garnet two-pyroxene granulite	Grt + Pl + Qtz + Kfs + Cpx + Opx	$\mathbf{Zrn} + \mathbf{Rtl} + \mathbf{Ap} + \mathbf{Ilm}$	Lower crust
W3S-1	Garnet two-pyroxene granulite	Grt + Pl + Qtz + Cpx + Opx	Zrn+Rtl+Ap	Lower crust
Kisite (2°50′25″S, 36°00′56	0"E)			
KS04-01	Orthogneiss	Pl + Qtz + Kfs + Opx + Bt + Gr t + Cc	$\mathbf{Zrn} + \mathbf{Rtl} + \mathbf{Ilm}$	Middle crust
KS04-10	Garnet two-pyroxene granulite	Pl + Qtz + Opx + Cpx + Grt	Ttn + Rtl	Lower crust
Pello Hill (2°45′54″S, 36°0	1′05″E)			
PH04-02	Amphibolite	Pl + Qtz + Hbl + Bt	Zrn+Ttn+Ap	Middle crust
PH04-05	Garnet two-pyroxene granulite	Pl + Grt + Cpx + Opx + Qtz	Zrn+Rtl	Lower crust
Eledoi (2°45′25″S, 36°01′40	O"E)			
EL04-01	Orthogneiss	Pl + Qtz + Kfs + Bt	Zrn+Mnz+Ap	Middle crust
Arusha area				
Lashaine (3°22′10″S, 36°25	''30"E)			
89-733	Garnet biotite two-pyroxene granulite	Grt + Pl + Cpx + Opx + Hbl + Bt	$\mathbf{Zrn} + \mathbf{Ap}$	Middle crust
89-745	Garnet biotite two-pyroxene granulite	Grt + Pl + Cpx + Opx + Hbl + Bt	Zrn+Ap	Middle crust
89-729	Garnet clinopyroxene granulite	Grt + Pl + Cpx	Ttn + Rtl + Ap + Ky	Lower crust
89-731	Garnet clinopyroxene granulite	Grt + Pl + Cpx	Ttn + Rtl + Ap + Ky	Lower crust
LS04-09	Garnet clinopyroxene granulite	Grt + Pl + Cpx	Rtl	Lower crust
Lemugur (3°26′30″S, 36°32	2′30″E)			
LG04-09	Schist	Grt + Pl + Qtz + Kfs + Bt + Ms	Zrn+Mnz+Rtl+Ap	Middle crust
LG04-37	Amphibolite	Pl + Qtz + Kfs + Hbl + Bt	$\mathbf{Zrn} + \mathbf{Ttn} + \mathbf{Ap}$	Middle crust
LG04-35	Garnet clinopyroxene granulite	Grt+Pl+Cpx	Rtl	Lower crust



Table 1 (continued)

Sample locations and names	Rock type	Major phases	Accessory phases	Present-day crustal level
LG04-38	Garnet two-pyroxene granulite	Grt + Pl + Cpx + Opx	Rtl	Lower crust
Loljoro (3°27′09″S, 36°36′2	23"E)			
LJ04-08	Quartzite	Pl + Qtz + Kfs + Bt + Ms	Zrn+Mnz+Rtl+Ap	Middle crust
LJ04-26	Orthogneiss	Pl + Qtz + Kfs + Bt	Zrn+Ttn+Ap	Middle crust
Olmani (3°23′50″S, 36°45′2	20"E)			
OM04-13	Orthogneiss	Pl + Qtz + Cpx + Grt + Bt	Zrn+Ttn+Ap	Middle crust
Mozambique Belt: Eastern G	ranulite cover			
Loibor Serrit (4°10′59″S, 36	6°24′45″E)			
LR04-05	Two-pyroxene granulite	Pl + Qtz + Kfs + Cpx + Opx + H bl + Bt	Zrn+Ap	Upper crust
LS06-01	Orthogneiss	Pl + Qtz + Kfs + Cpx + Hbl + Bt	Zrn+Ap	Upper crust
LS06-02	Orthogneiss	Pl + Qtz + Kfs + Cpx + Hbl + Bt	Zrn+Ap	Upper crust
LR04-01	Garnet two-pyroxene granulite	Grt + Pl + Qtz + Kfs + Cpx + Opx	Zrn+Ap	Upper crust
LS06-12	Garnet clinopyroxene granulite	Grt + Pl + Cpx	$\mathbf{Zrn} + \mathbf{Ttn} + \mathbf{Rtl} + \mathbf{Ap}$	Upper crust
Mozambique Belt: Western C	Granulites			
Longido (2°46'28"S, 36°30'	′13″E)			
LK06-02	Orthogneiss	Grt + Pl + Qtz + Opx + Hbl + Bt	Zrn+Ttn+Ap	Upper crust
Magugu (3°49′31″S, 35°50′	5"E)			
MG04-01	Orthogneiss	Grt + Pl + Qtz + Opx + Hbl + Bt	$\mathbf{Zrn} + \mathbf{Rtl} + \mathbf{Ap}$	Upper crust

Italicized samples are ones described in Mansur et al. (2014). Petrochronological data is presented for phases in bold lettering. Crustal levels for xenoliths are inferred using major-element thermobarometry and/or pseudosection models

Mineral abbreviations: Ap apatite, Bt biotite, Cc calcium carbonate, Chl chlorite, Cpx clinopyroxene, Ep Epidoite, Grt garnet, Hbl hornblende, Ilm ilmenite, Kfs K-feldspar, Ky kyanite, Mnz monazite, Ms muscovite, Opx orthopyroxene, Pl plagioclase, Qtz quartz, Rtl rutile, Tm titanite, Zrn zircon

the margin of the Tanzanian Craton (Labait) and multiple sites in the EAO (Fig. 1; Table 1). All surface samples come from outcrops within the orogen. To distinguish high-grade rocks from the Western/Eastern Granulites at the surface from deep crustal xenoliths erupted on the EAO, we refer to the former as the Mozambique Belt (upper plate and part of the lower plate of the EAO; Fig. 1) and the latter the lower plate of the EAO. Individual petrographic descriptions are presented in the Supplementary Materials.

Labait xenoliths

The analyzed suite of Labait xenoliths consists of ten samples—granite, schist, amphibolite, and granulites—interpreted to sample the upper–lower crust (Table 1). One granite xenolith is undoubtedly from the upper crust. In contrast, it is difficult to be certain of derivation depths of a schist and two amphibolite xenoliths largely because they lack diagnostic phase assemblages (Table 1). However, because the craton surface is dominated by granitoids, syenites, and orthogneisses, we infer that these xenolith lithologies are from mid-crustal depths, though this is not required.

Additionally, pseudosection modeling for one amphibolite xenolith (sample LB04-89) indicates equilibration pressures of < 1 GPa and < 450 °C (Fig. S4), corroborating a mid-crustal origin. Six granulite xenoliths derive from lower crustal depths. Thermobarometry and pseudosection modeling of two-pyroxene gabbroic granulite xenoliths indicated equilibration at > 750 °C and < 1.0–1.2 GPa (Mansur et al. 2014). Garnet-orthopyroxene granulites equilibrated at higher pressures (1.0–1.6 GPa) and are interpreted to be derived from the lowermost crust of the craton (Mansur et al. 2014).

Table 1 reports the occurrence of pertinent accessory phases: all samples contain zircon; apatite is present in all samples except the garnet-bearing granulites; and rutile is present in the three garnet-bearing granulites and in one amphibolite xenolith (Table 1). Titanite and monazite are not present in the analyzed samples.

Natron area xenoliths

We have analyzed ten xenoliths from Naibor Soito, Kisite, Pello Hill, and Eledoi (Fig. 1), which we refer to collectively as the Natron group. The Natron group xenoliths



include orthogneisses, amphibolites, and granulites. As is the case for the Labait xenolith suite, the absence of key phases, like garnet, in the orthogneiss and amphibolite xenoliths and the occurrence of high-grade lithologies at the surface (Fig. 1) complicates interpretations of the derivation depths of these xenoliths. Pseudosection modeling of one amphibolite (sample LJ04-26) and one orthogneiss (sample OM04-13) indicates maximum pressures of 0.6–0.8 GPa (see Fig. S4)—consistent with a mid-crustal origin for these samples.

Granulite xenoliths sample the lower crust. Naibor Soito granulite xenoliths have variable mineral assemblages (Table 1), but thermobarometry and pseudosection modeling are all consistent with equilibration at > 700 °C and > 1 GPa (Mansur et al. 2014). Mafic garnet granulites from Kisite and Pello Hill are similar to those from Naibor Soito and are thus also interpreted to be from the lower crust.

Zircon is present in nine xenoliths and apatite is present in seven xenoliths (Table 1). Rutile and titanite occur in a few samples; the former is found in six garnet granulite xenoliths (but only analyzed in five samples), and the latter is present in one amphibolite and in one mafic garnet granulite where it overgrows rutile. Monazite occurs in one orthogneiss (Table 1).

Arusha area xenoliths

We analyzed 12 xenoliths from Lashaine, Lemugur, Loljoro, and Olmani, referred to herein as the Arusha group. Rocks in this suite include orthogneisses, quartzites, schists, amphibolites, and granulites. Like the Natron group xenoliths, we infer that the orthogneiss, quartzite, schist, and amphibolite xenoliths are from the middle crust (rather than the upper crust). Granulite xenoliths from Lashaine are dominantly mafic and contain garnet (Table 1). Based on thermobarometry and pseudosection calculations and the presence of kyanite and garnet coronae, garnet granulites are inferred to have equilibrated at the base of a thickened crustal section (~ 800 °C to > 1200 °C and 1.3 to > 1.7 GPa; Jones et al. 1983; Mansur et al. 2014). Thermobarometry of biotitegarnet granulites suggest equilibration temperatures and pressures lower than biotite-free garnet granulites (~600 °C and < 0.8 GPa; Mansur et al. 2014), indicating a shallower (likely mid-crustal) origin for biotite-garnet granulite xenoliths (Table 1).

Zircon is observed in all samples except for the biotitefree mafic garnet granulites (Table 1). Apatite is present in seven samples. Monazite is found in one schist and one quartzite xenoliths. Rutile is present in most of the mafic garnet granulites and in the schist and quartzite xenoliths. Titanite is found in one orthogneiss and in two garnet granulites (Table 1).

Surface samples

To obtain a more complete picture of the thermal history of the crust, we analyzed seven high-grade metamorphic rocks exposed at the surface of the East African Orogen. These include intermediate—mafic granulites and orthogneisses that were metamorphosed at mid—lower crustal depths during orogeny before being exposed at the surface through post-orogenic uplift and erosion (e.g., Appel et al. 1998; Möller et al. 2000; Cutten et al. 2006).

Surface samples come from three areas in the Mozambique Belt: Loibor Serrit, Magugu, and Longido (Fig. 1). Except for sample LS06-12, which is a river cobble, all surface samples were collected from outcrops. Loibor Serrit is situated within the Eastern Granulite cover (Tenczer et al. 2013). Samples from Loibor Serrit are metaigneous granulites containing clinopyroxene + plagioclase ± orthopyroxene ± quartz ± hornblende ± biotite ± garnet (some with clinopyroxene rims) (Table 1). Samples from Longido and Magugu come from the Western Granulites. Although Longido is mapped as being within the Eastern Granulite cover (Fritz et al. 2005), it likely represents a window into the Western Granulites (Tenczer et al. 2013). The Longido and Magugu samples are both foliated orthogneisses containing garnet + plagioclase + quartz + orthopyroxene ± hornblende \pm biotite (Table 1).

All surface samples contain zircon and apatite (Table 1). Rutile is present in Loibor Serrit sample LS06-12 and Magugu sample MG04-01. Titanite is also present in LS06-12, which also contains rutile, and in Longido sample LK06-02.

Materials and methods

Laser-ablation split-stream ICP-MS (LASS) U-Pb and trace element analyses

Accessory phases were separated at UCSB using standard crushing, magnetic and heavy liquid separation methods. LASS analyses utilized a Cetac Teledyne 193 nm excimer Analyte laser with a HelEx ablation cell coupled to two mass spectrometers: a multicollector (MC)-ICPMS for U-Pb dating and a quadrupole (Q)-ICPMS for simultaneous trace element determinations (following procedures modified from Kylander-Clark et al. 2013). A Nu Instruments Plasma HR-ES MC-ICP multicollector was used for data obtained in the first phase of the project, and a Nu Instruments Plasma 3D MC-ICP for later analyses. Trace elements were acquired using an Agilent 7700S Q-ICP. LASS analyses were done in two ways: conventional LASS spot analyses on polished crystal interiors or depth profiling of whole grains. Details



of LASS protocols, data reduction, and error propagations are presented in the Supplementary Materials.

U-Pb and trace element petrochronology

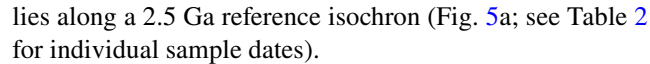
Simultaneously collected U–Pb and trace-element data can discriminate among thermally-mediated volume diffusion, recrystallization, and neocrystallization (new mineral growth during metamorphism). While a large suite of trace elements was analyzed in each mineral (see Tables S4-S8), we only discuss elemental data pertinent to tracking changes in pressure, temperature, and stable mineral assemblages, or data for elements with known diffusivities for comparison with U–Pb zonations. These include: rare earth elements (REEs) in zircon, monazite, titanite, and apatite (e.g., Bingen et al. 1996; Rubatto 2002; Spear and Pyle 2002; Whitehouse and Platt 2003; Taylor et al. 2015; Garber et al. 2017; Henrichs et al. 2019); Hf in zircon; Sr in apatite (Ague and Baxter 2007); and various 4+cation thermometers—Ti-in-zircon (TiZ), Zr-in-titanite (ZiT), and Zr-in-rutile (ZiR) (Ferry and Watson 2007; Hayden et al. 2008; Tomkins et al. 2007; Taylor-Jones and Powell 2015). An in-depth discussion of the systematics and our applications of these different trace element monitors is presented in as Supplementary Materials.

Results

Our dataset consists of depth profiles and spot analyses for a variety of accessory minerals. In most cases, spot analyses were able to date rims that were also sampled by depth profiling (see Fig. 2 for examples of zircon rims). Because spot analyses have lower uncertainties associated with both their U–Pb and trace-element compositions (Table S2), we refer to them in our plots and discussion. Where depth profiling uniquely captured an age or compositional gradient, we present depth profile data separately from spot analyses. Data are reported in Tables S6–S10.

Labait xenoliths (craton margin)

Zircon, rutile, and apatite in upper–middle crustal xeno-liths at Labait—one granite, one schist, and two amphibolites (Table 1)—record Archean dates. Zircon in the granite and schist is generally metamict and highly discordant (Table S7), but in amphibolite xenoliths LB04-89 and LB04-92 zircon yields concordant dates of 2.68 ± 0.17 Ga and 2.65 ± 0.04 Ga, respectively (Table 2). Zircon has uniform trace-element compositions (Fig. 3) and records TiZ temperatures of ~680 °C (Table 2). Rutile in one amphibolite xenolith (LB04-89) yields an Archean lower intercept date of 2.63 ± 0.03 Ga (Fig. 4) and exhibits ZiR temperatures between 520 and 730 °C (Table 2). Apatite in these xenoliths



Zircon, rutile, and apatite in Labait granulite xenoliths yield variable U-Pb and trace element data. Cathodoluminescence (CL) imaging of polished zircon grains from the granulite xenoliths reveals multiple growth domains in the form of thick overgrowths that mantle small (<40 µm), dark cores with strong sector zoning (Fig. 2a). In the three, twopyroxene granulites, U-Pb zircon dates range from 2.8 to 2.6 Ga (Fig. 3a). Decreased Eu/Eu* and increased Ti contents—indicative of temperatures up to 940 °C—correspond to younger dates (Fig. 3b, E). Zircon in three garnet-bearing granulites records dates that are slightly younger—mostly 2.76–2.54 Ga (Fig. 3a). Ti contents suggest temperatures that extend well into ultra-high temperatures (UHT; > 900 °C) at ca. 2.64 Ga (Fig. 3c). Zircon in the garnet granulites also documents elevated Gd/Yb_N and lower Lu/Hf across the same time interval, consistent with growth in the presence of garnet during this UHT event (Fig. 3b).

Rutile in Labait garnet-bearing granulites displays complex age and elemental patterns. Most rutile grains have low U (<1 ppm), making it difficult to extract dates from depth profiles (see Supplementary Materials); we instead focus on spot analyses. Further complicating matters is that backscattered electron (BSE) imaging and energy-dispersive X-ray spectroscopy (EDS) reveals networks of fine zircon exsolution lamellae in some grains (Fig. 2d). Spot analyses with elevated Si (> 700 ppm) likely represent contamination from zircon exsolution lamellae and are filtered from the final rutile dataset (see Fig. S8). A subset of analyses lies near concordia at 600-500 Ma (inset in Fig. 4b), though most are largely discordant (Fig. 4b). Common-Pb corrected dates from the filtered dataset range are 600 Ma to < 20 Ma (Fig. 4b) with one datum at ca. 2.5 Ga and another at ca. 1.2 Ga. Concentrations of Zr vary by almost two orders of magnitude in rutile (100–8000 ppm) corresponding to temperatures between 500 and 900 °C (Fig. 4c), but do not correlate with U-Pb date (Fig. 4d).

Apatite in two-pyroxene granulites show distinct U–Pb trends: in one sample (intermediate granulite LB04-36), the data lie along a 2.5-Ga reference isochron and diverge towards younger dates (Fig. 5b), and in another sample (mafic granulite LB04-82), the data scatter about a 400-Ma reference isochron, but also show mixing with an older, Archean-age component (Fig. 5c). Depth profiles reveal the presence of discrete young (down to 10 Ma), < 5 µm-thick overprints on the edges of grains (Fig. 5d, e). Concomitant with changes in U–Pb dates are shifts in LREE and Sr contents. CL imaging of the dated grains reveals an intricate network of dark patches around grain rims and along cracks (Fig. 2e) typically observed in phases that have undergone partial dissolution/reprecipitation (e.g., Corfu et al. 2003; Harlov et al. 2005; Holder and Hacker 2019).



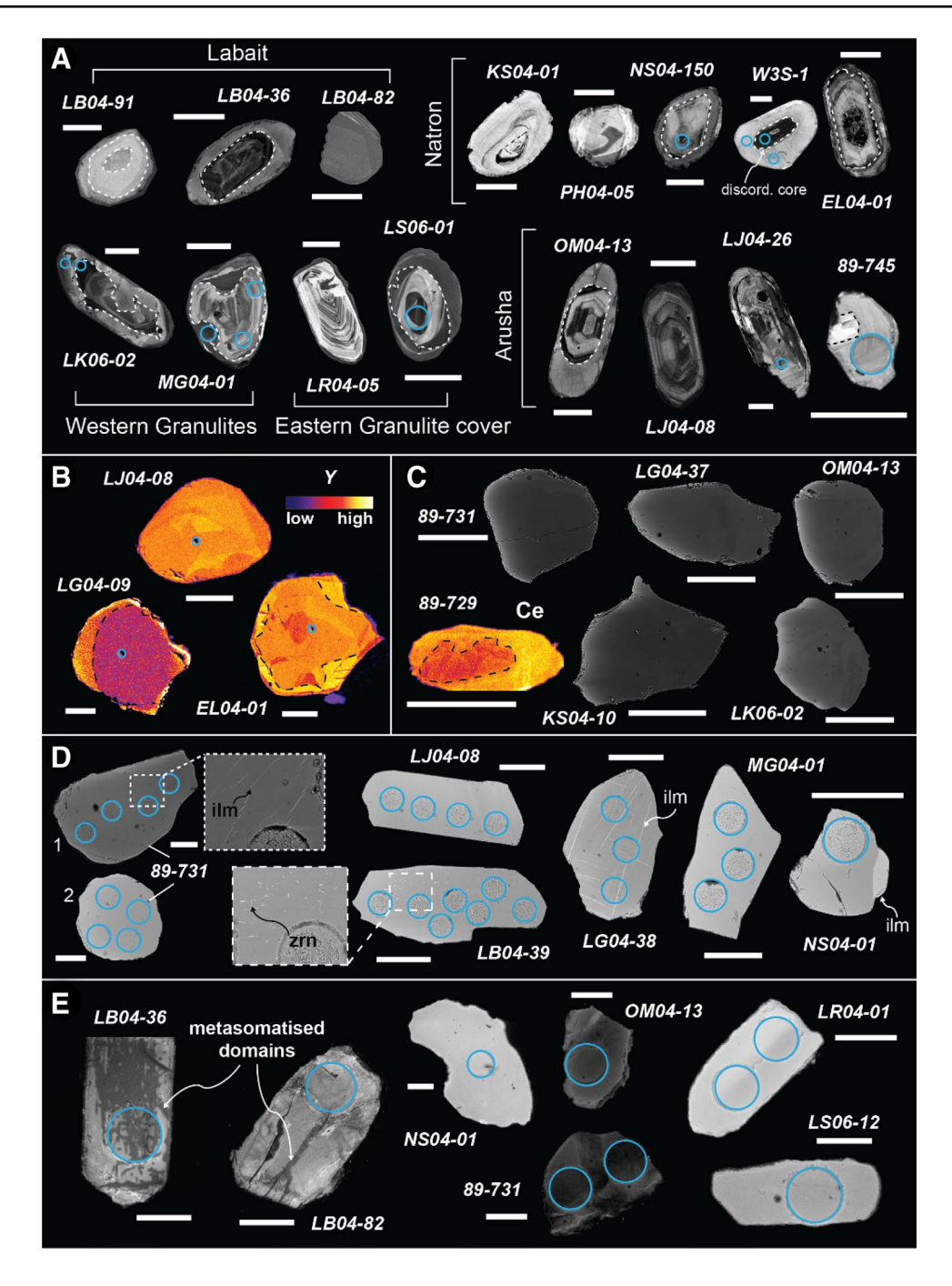


Fig. 2 Images of representative grains analyzed. White bars are 50 μm wide. Blue circles represent laser spots. **a** Representative zircon grains (CL). Rims are denoted in dashed lines. See text for discussion of different rim/core dates. **b** Qualitative Y intensity maps of representative monazite grains. Despite the faint variations in Y concentrations within monazite from samples LJ04-08 and LG04-09, all dates are consistently Neoproterozoic. Monazite from sample EL04-01 yielded Neoarchean and Neoproterozoic dates; the former is associated with brighter patches around the rim. Other element maps are shown in Supplementary Materials. **c** Representative titanite grains (X-ray and BSE). Qualitative Ce intensity maps of a titanite grain from sample 89-729 clearly shows a core and mantle. Titanite grains in other granulite xenolith show faint internal structures in BSE, suggesting they too contain complexities. Titanite grains in mid-crustal xenoliths and surface outcrops appear to lack any apparent zonations

in BSE, consistent with U–Pb and trace-element data. **d** Representative rutile grains (BSE). Rutile from off-craton garnet granulite xenoliths (89-731 grain 1, LG04-38, and NS04-01) contain fine ilmenite exsolution lamellae or ilmenite overgrowths (although not all grains do, e.g., 89-731 grain 2). Rutile from on-craton garnet granulites often contain zircon exsolutions like those shown in LB04-39. Rutile grains from mid-crustal xenoliths (LJ04-08) and surface outcrops (MG04-01) are devoid of any exsolutions. **e** Representative apatite grains. Note the complex structure in grains from Labait granulite xenoliths, consistent with the variable U–Pb dates observed. Darker patches in the apatites are interpreted to have formed via melt interactions during or slightly before eruption. Apatite from other garnet granulite xenoliths (NS04-01), mid-crustal xenoliths (mid-crustal; OM04-13), and surface outcrops (LR04-01 and LS06-12) lack any apparent internal structure



 Table 2
 Summary of petrochronologic data

Sample	Rock type	Phase	Best dates (Ma) ^a	$\pm 2\sigma (n)^{b}$	T estimates ^c (°C)	$\pm 2\sigma (n)^{d}$	Notes
Tanzanian Crat	on						
Labait	~ .	_					
LB04-86	Granite	Zrn	Discordant	_	_		Metamict
		Ap	2525	31 (21)			
LB04-05	Schist	Zrn	Discordant	_	_		Metamict
		Ap	2496	30 (25)			
LB04-89	Amphibolite	Zrn	2678	17 (1)	680	40 (1)	Single concordant point
		Rtl	2621	31 (22)	520–730	– (24)	
I DO4 02	A 1.9 19	Ap	2533	40 (21)	600	10 (05)	
LB04-92	Amphibolite	Zrn	2649	4 (22)	680	10 (25)	
I DO4 26	Two manages amounties	Ap Z	2560	47 (18)	770	10 (20)	
LB04-36	Two-pyroxene granulite	Zrn	2840–2587	(20)	770	10 (39)	LDEE amaighed aims
I DO4 10	Two manages amounties	Ap Z	2600-0	- (29)	040	10 (20)	LREE enriched rims
LB04-19	Two-pyroxene granulite	Zrn	2725–2598	– (27)	940	10 (29)	Low U U b.d.l
LB04-82	Two-pyroxene granulite	Ap Zrn	- 2728–2612	- - (24)	810	20 (24)	U U.d.1
LD04-62	rwo-pyroxene granume	Ap	1200–340	- (24) - (23)	810	20 (24)	LREE enriched rims
LB04-91	Garnet orthopyroxene	Zrn	2761–2595	- (23) - (44)	920	10 (45)	LREE chilched this
LB04-91	granulite					10 (43)	
I DO 1 20	G	Rtl	Discordant	- (30)	-	10 (22)	
LB04-39	Garnet orthopyroxene granulite	Zrn	3027–2537	- (28)	950	10 (33)	
		Rtl	Discordant	– (24)	-		
LB04-74	Garnet orthopyroxene granulite	Zrn	2619–2572	– (8)	780–915	– (8)	
		Rtl	Discordant	- (24)	_		
Natron area							
Naibor Soito							
NS04-96	Two-pyroxene granulite	Zrn	2703–2520	– (8)	820	10 (36)	
		Ap	11	17 (19)			
NS04-150	Two-pyroxene granulite	Zrn	2717–2484	– (20)	780	10 (44)	
		Ap	2.4	10 (20)			
NS04-60	Garnet two-pyroxene granulite	Zrn	2696–2567	– (6)	760	10 (21)	Discordant cores
		Rtl	0.1	0.1 (15)	N/A		
		Ap	1.5	2.1 (15)			
NS04-01	Garnet two-pyroxene granulite	Zrn	2880–2599	– (21)	780	10 (40)	
		Rtl	0.1	0.1 (18)	770	10 (18)	
		Ap	0.0	1.4 (22)			
W3S-1	Garnet two-pyroxene granulite	Zrn	2690–2528	- (6)	820	10 (37)	
		Rtl	0.1	0.1 (18)	690	10 (18)	
		Ap	0.8	2.5 (25)			
Kisite		•					
KS04-01	Orthogneiss	Zrn	2862-2585	– (5)	760	10 (25)	
KS04-10	Garnet two-pyroxene granulite	Ttn	540–440	- (38)	770	10 (38)	
	-	Rtl	0.4	0.3 (27)	N/A		No zrn in sample
Pello Hill				. ,			•
PH04-02	Amphibolite	Zrn	588	9 (3)	670	30 (3)	



Table 2 (continued)

Sample	Rock type	Phase	Best dates (Ma) ^a	$\pm 2\sigma (n)^{b}$	T estimates ^c (°C)	$\pm 2\sigma (n)^{\rm d}$	Notes
		Ttn	533	7 (33)	760	10 (34)	
		Ap	524	30 (16)			Low U
PH04-05	Garnet two-pyroxene granulite	Zrn	2591–2461	- (28)	N/A		No Qtz in sample
		Rtl	2.6	0.9 (20)	N/A		No Qtz in sample
Eledoi							
EL04-01	Orthogneiss	Zrn	2737–2666	-(15)	740	10 (15)	Younger, discordant rims
		Mnz	2633	5 (20)			
			546	12 (1)			Single concordant depth profile analysis
		Ap	467	10 (23)			
Arusha area							
Lashaine							
89-733	Garnet biotite two-pyroxene granulite	Zrn	2560	18 (1)	770	50 (1)	Single concordant core date
			607	9 (3)	710	40 (3)	
89-745	Garnet biotite two-pyroxene granulite	Zrn	581	8 (3)	690	30 (3)	
		Ap	487	14 (23)			
89-729	Garnet clinopyroxene granulite	Ttn	560–330	- (29)	740	10 (29)	T is maximum (assuming $aSiO_2 = 1$, but no Qtz in rock)
		Rtl	0.7	0.6 (23)	N/A		No Zrn or Qtz in sample
		Ap	_	_			U b.d.l
89-731	Garnet clinopyroxene granulite	Ttn	550–260	- (33)	730	10 (33)	T is maximum (assuming aSiO2=1, but Qtz in rock
		Rtl	1.8	0.6 (20)	N/A		No Zrn or Qtz in sample
Lemugur		Ap	_	_			U b.d.l
LS04-09	Garnet clinopyroxene granulite	Rtl	0.5	0.1 (49)	N/A		No Zrn or Qtz in sample
LG04-09	Schist	Zrn	Discordant	_	_		Metamict
		Mnz	605–567	- (56)			High Y rims compared to cores
		Rtl	500	4 (27)	710	10 (27)	
		Ap	444	24 (16)			
LG04-37	Amphibolite	Zrn	2530	10 (10)	740	20 (10)	Younger, discordant rims
		Ttn	540–480	- (35)	770	10 (35)	
LG04-35	Garnet clinopyroxene granulite	Rtl	1.0	0.6 (26)	N/A		No Zrn or Qtz in sample
LG04-38	Garnet clinopyroxene granulite	Rtl	-	-	N/A		U b.d.l.; no Zrn or Qtz in sample
Loljoro							
LJ04-08	Quartzite	Zrn	3479–2661	- (13)	700	10 (13)	Younger, discordant rims
		Mnz	588	2 (28)			
		Rtl	498	3 (58)	700	10 (58)	
1.104.24	0.4	Ap	473	13 (28)	600	20 (2)	
LJ04-26	Orthogneiss	Zrn	2519	10 (3)	690	30 (3)	0. 1
			643	13 (1)	_		Single concordant depth profile analysis
		Ttn	528	9 (56)	750	10 (56)	
		Ap	499	15 (20)			



Table 2 (continued)

Sample	Rock type	Phase	Best dates (Ma) ^a	$\pm 2\sigma (n)^{b}$	$T \ estimates^c \ (^{\circ}C)$	$\pm 2\sigma (n)^{\rm d}$	Notes
OM04-13	Orthogneiss	Zrn	2706	9 (5)	700	20 (5)	
	-		607	6 (6)	700	20 (6)	
		Ttn	514	10 (38)	770	10 (38)	
		Ap	480	19 (23)			
Mozambique I	Belt: Eastern Granulite cover						
Loibor Serrit							
LR04-05	Two-pyroxene granulite	Zrn	917-732	-(18)	720	10 (18)	
		Ap	507	6 (23)			
LS06-01	Orthogneiss	Zrn	728-645	- (20)	730	10 (20)	
		Ap	498	4 (24)			
LS06-02	Orthogneiss	Zrn	905-722	- (23)	710	10 (23)	
		Ap	521	6 (25)			
LR04-01	Garnet two-pyroxene granulite	Zrn	773–642	-(10)	720	10 (10)	
		Ap	513	8 (27)			
LS06-12	Garnet two-pyroxene granulite	Zrn	890–632	- (30)	640–830	- (30)	
		Ttn	614	3 (23)	860-900	- (23)	Cross calibrated ZiR and ZiT
		Rtl	568	18 (6)	860-900	-(6)	Cross calibrated ZiR and ZiT
		Ap	458	7 (26)			
Mozambique I	Belt: Western Granulites						
Longido							
LK06-02	Orthogneiss	Zrn	2516	6 (10)	750	30 (10)	
			613	4 (15)	620	20 (15)	
		Ttn	543	13 (38)	750	10 (38)	
		Ap	457	25 (19)			Low U
Magugu							
MG04-01	Orthogneiss	Zrn	2944, 2422	20, 17 (2)	760	30 (2)	
			630	16 (1)	530	90 (1)	Single concordant date; large T uncertainty
		Rtl	515	8 (6)	680	20 (6)	
		Ap	510	9 (26)			

Mineral abbreviations same as in Table 1

Mozambique belt outcrops

Zircon from five samples of the Eastern Granulite cover locality at Loibor Serrit records concordant U-Pb dates ranging from 920 to 640 Ma (Fig. 6a). Zircon in garnetabsent two-pyroxene granulites and orthogneisses shows relatively constant Gd/Yb_N, Ti, and Th/U, but lower Eu/ Eu* at 750-640 Ma. In garnet-bearing granulites, zircon records a spread of dates from 890 to 630 Ma and shows greater variations in trace elements (dark blue diamonds in Fig. 6b-e). Temperatures range from ~830 °C to 650 °C



^aBest dates for zircon and monazite are dates within 5% concordance (between ²³⁸U/²⁰⁶Pb and ²⁰⁷Pb/²⁰⁶Pb dates), and ²⁰⁷Pb-corrected U-Pb dates for titanite, rutile, and apatite (applying common Pb compositions reported in Table S3)

^bUncertainities are internal only. Dates reported outside this study should adopt uncertainities associated with long-term reproducibilty of analyzed homogeneous lab standards (1-3%; see Supplements for details). Dash denotes data that does not conform to a single population; n is the number of data used to calculate mean and 2σ uncertainty, or number of data in specified range

^cCalculated using 4+cation thermometers of Ferry and Watson (2007) for zircon, Tomkins et al. (2007) for rutile, and Hayden et al. (2008) for titanite. Temperatures are averages, unless where shown as ranges, and rounded up

^dUncertainties for temperatures account for analytical uncertainties and uncertainties in Si and Ti activities (± 0.1), but not thermometer calibrations. Pressures of 1 GPa for granulites and 0.6 GPa for amphibolites and orthogneisses are used for temperature calculations (assuming ±0.1 GPa uncertainty) (see Supplements for details). Dash denotes data that does not conform to a single population; n is the number of data used to calculate mean and 2σ uncertainty, or number of data in specified range

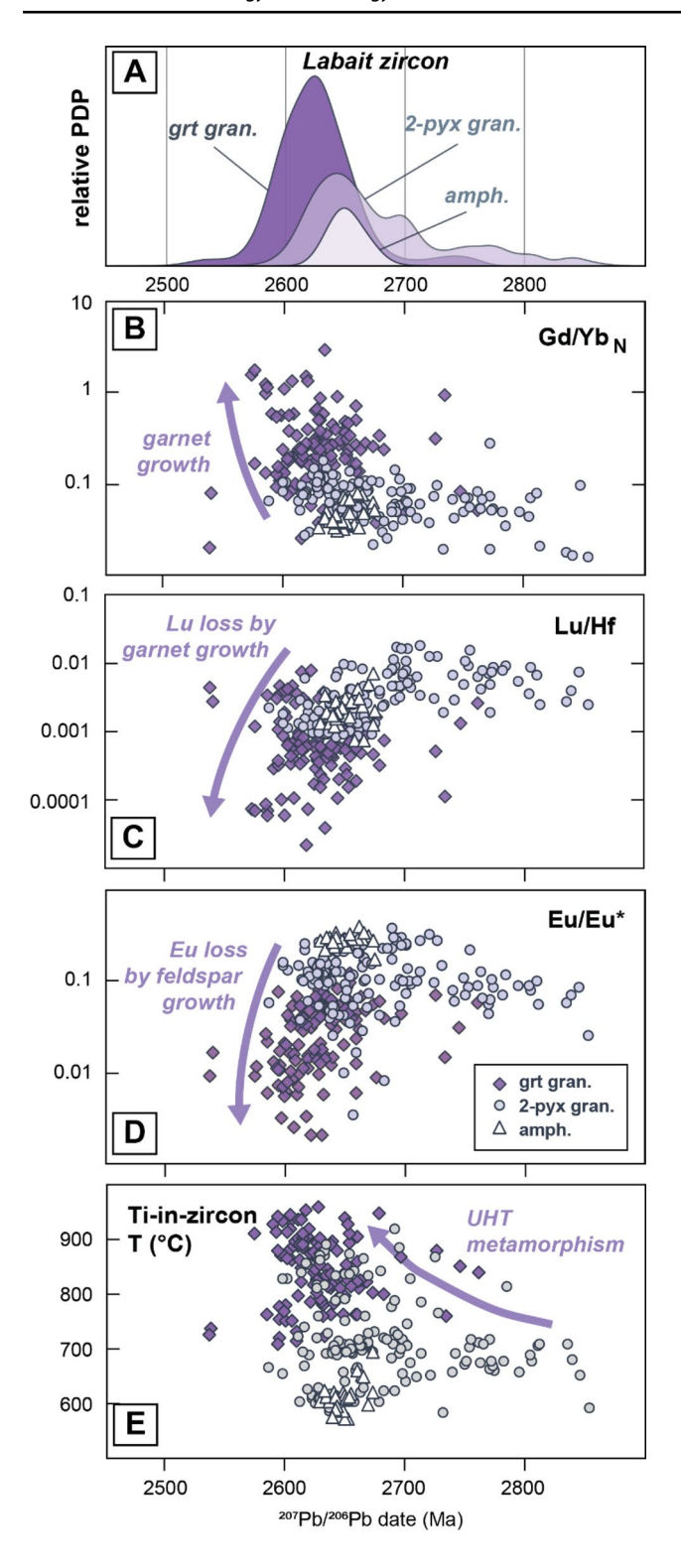


Fig. 3 Zircon petrochronology of Labait xenoliths. Only data points within 5% concordance are plotted. a Probability distribution plot (PDP) of zircon U–Pb dates from the different xenolith types. b–e Trace-element variations with zircon dates. Differences in trace-element patterns among the different samples occur at ca. 2.64 Ga and include increases in the chondrite-normalized (using values of McDonough and Sun 1995) Gd/Yb ratios and TiZ temperatures, as well as decreases in zircon Eu anomaly and Lu/Hf, which are attributed to growth of garnet and elemental fractionation by protracted zircon growth from a melt (see text for details)

from 780 to 610 Ma, Gd/Yb_N increases at 780–770 Ma, and Eu/Eu* decreases with decreasing age (Fig. 6b–e).

Titanite, rutile, and apatite in the Eastern Granulite cover are as young or younger than the youngest zircon dates (Fig. 7). Titanite and rutile in the same garnet-granulite (sample LS06-12) yield uniform U–Pb dates of 614 ± 3 and 568 ± 18 Ma, respectively. Application of the ZiR and ZiT thermometers in this sample yields overlapping temperatures of 860-900 °C at 1.0-1.4 GPa. Apatite U–Pb dates in all samples significantly post-date those of titanite and rutile, and dominantly fall along a 527-Ma reference isochron (Fig. 7F; see Table 2 for individual sample dates).

Dates from two orthogneisses of the Western Granulites at Magugu and Longido are Archean and Neoproterozoic (Table 2). Concordant zircon rim dates are 613 ± 4 Ma and 630 ± 16 Ma (5–40 µm-thick; Fig. 2a) and concordant zircon Archean cores dates are 2944 ± 20 , 2522 ± 17 Ma, 2420 ± 6 Ma (Table 2). The rims record relatively low TiZ temperatures and Th/U compared to older cores (Fig. 6d). Titanite in sample LK06-02 has an age of 543 ± 13 Ma (Fig. 7) with a ZiT temperature of ~750 °C (Table 2). Rutile in sample MG04-01 yields younger 515 ± 8 Ma dates (Fig. 7) and ZiR temperatures of ~680 °C (Table 2). Apatite in sample LK06-02 has an age of 457 ± 25 , and apatite in sample MG04-01 has an age of 510 ± 9 Ma, which overlaps in age with rutile from the same rock (Fig. 7).

Natron and Arusha xenoliths

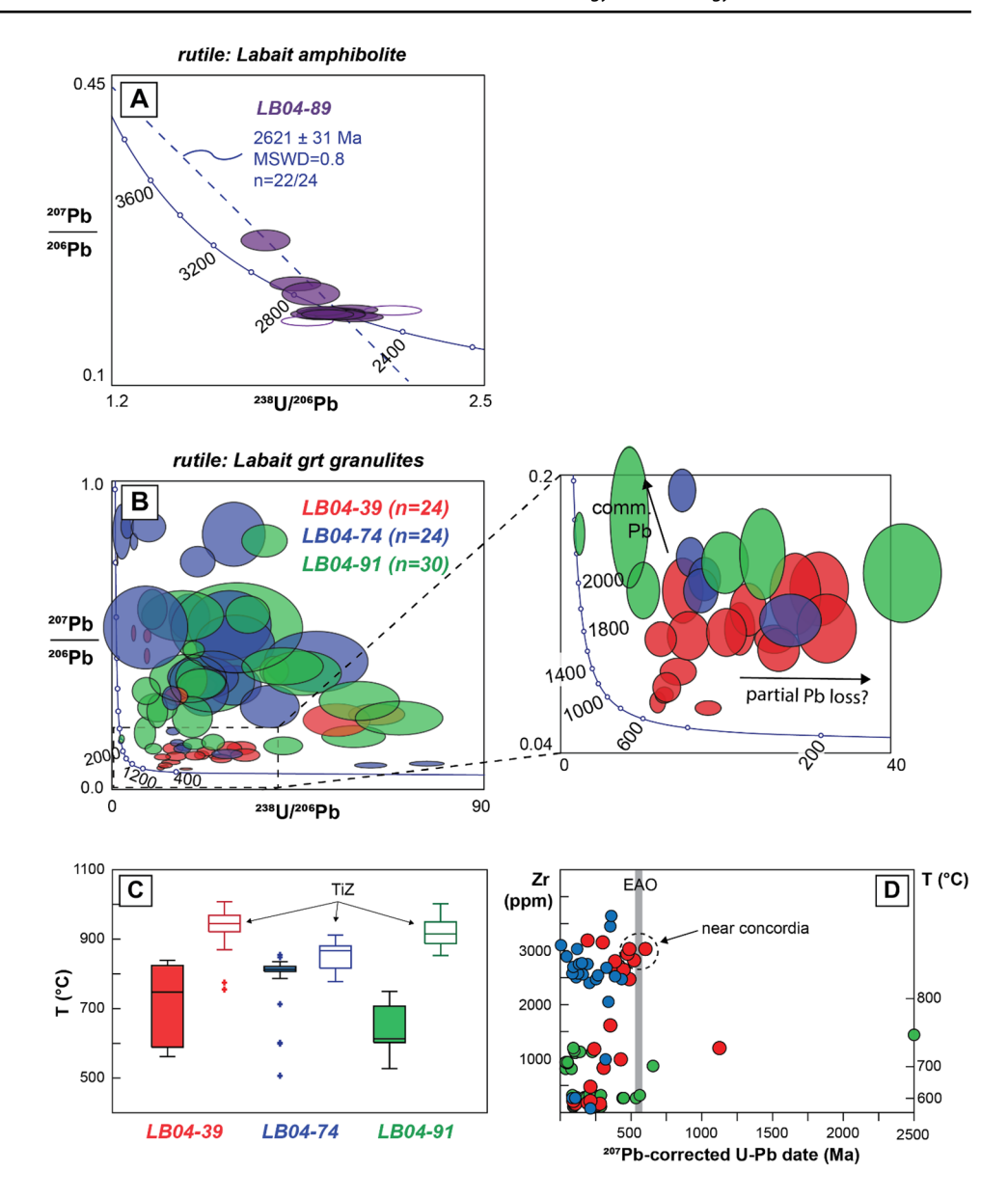
Crustal xenoliths from the Natron and Arusha areas contain accessory phases with a wide range of U–Pb and elemental compositions (Fig. 7). Given the large number of phases analyzed in the various xenoliths (see summary in Table 2), we focus on general trends in the data from middle (schists, amphibolites, orthogneisses, quartzites, etc.) and lower crustal (granulites) samples from the two xenolith regions.

Zircon in three mid-crustal xenoliths from the Natron area and seven mid-crustal xenoliths from the Arusha area yields Neoproterozoic dates, Archean dates, or both (i.e., Neoproterozoic rims around Archean cores) (Table 2). General compositional differences between the Archean and Neoproterozoic age groups include the following: lower Th/U and Ti and higher Gd/Yb $_{\rm N}$ in the latter, but other than these, there are no clear temporal trends in the zircon data (Fig. S9). Neoproterozoic dates in the mid-crustal xenoliths from both areas overlap with those from the Western Granulites (Table 2), but the xenoliths show a much larger range of Archean dates, including older populations at 3.0–2.6 Ga (Fig. S9).

Monazite is present in three mid-crustal xenoliths: a Natron orthogneiss (EL04–01) and in an Arusha quartzite (LJ04-08) and schist (LG04-09; Fig. 7). Qualitative X-ray maps reveal core—rim differences in REEs and Y (Fig. 2b;



Fig. 4 Labait rutile data. a Tera-Wasserberg concordia plot of rutile spot analyses from amphibolite xenolith LB04-89. Data are not common-Pb corrected. b Tera-Wasserberg concordia plot of all rutile spot analyses from garnet granulite xenoliths (colored by sample). Rutiles in all samples show a similarly large age range. The inset shows a subset of analyses that lie near concordia at 600-500. Data are not common-Pb corrected. c Box-and-whisker plot comparing ZiR (filled) and TiZ (unfilled) temperatures in the different garnet granulite xenoliths. Note how ZiR temperatures are lower. d Common-Pb corrected U-Pb date vs. Zr contents. No discernable correlation exists in any of the samples. Same color scheme as in panels b/c



S18). Spot analyses of monazite in Natron orthogneiss sample EL04-01 show Archean cores that record minor mixing with a Neoproterozoic component; a Neoproterozoic rim is confirmed by depth profiling (546 ± 12 Ma; Table 2) and by chemical dates (Table S5). In Arusha quartzite sample LJ04-08, spot analyses from different monazite grains yield a single age population (588 ± 2 Ma). In Arusha schist sample LG04-09, spot analyses of distinct compositional zones yield dates ranging from 605 to 567 Ma and show increasing Y and decreasing Gd/Yb_N with younger dates (Fig. S10).

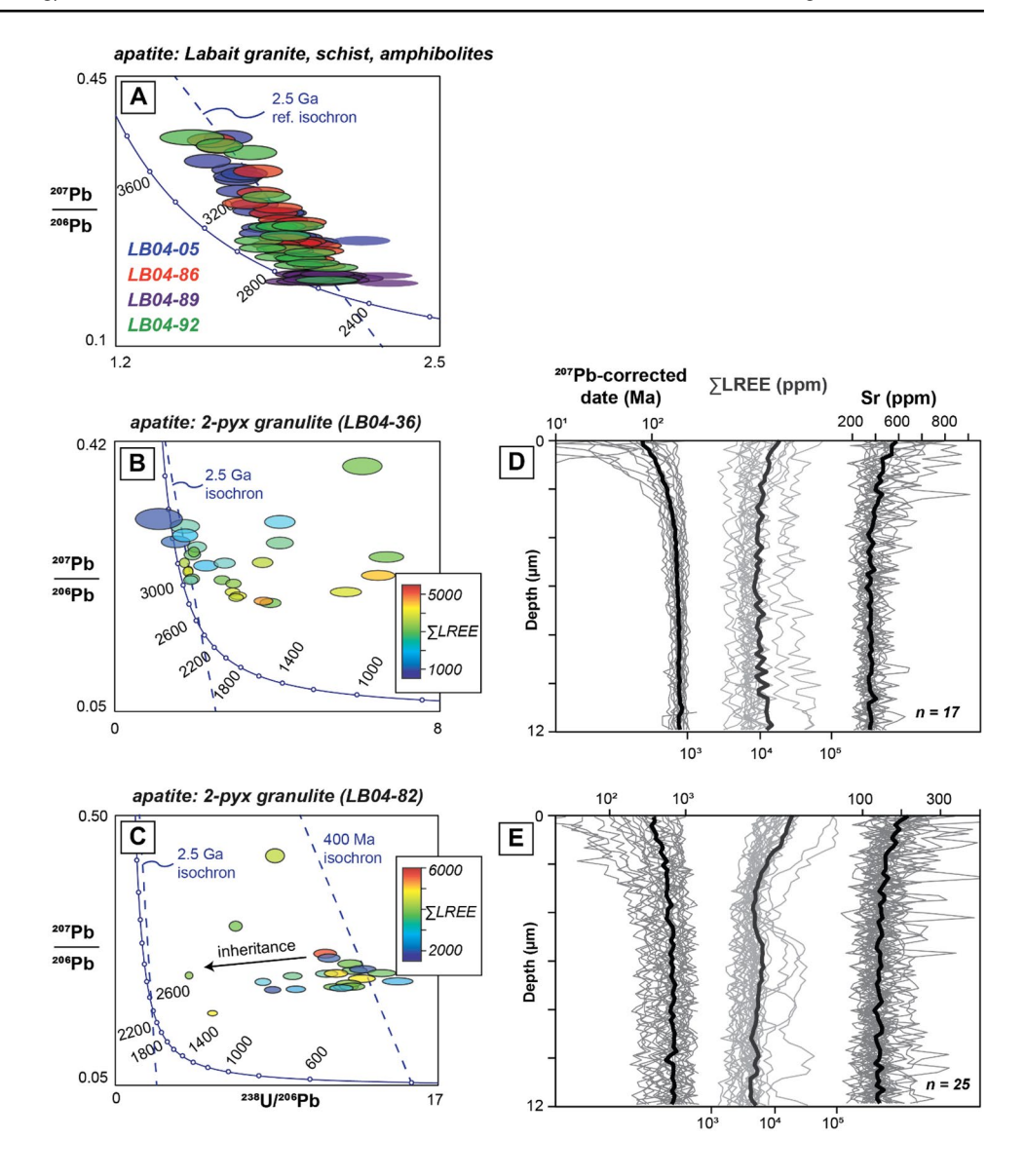
Titanite, rutile, and apatite in mid-crustal xenoliths from the Natron and Arusha groups are Neoproterozoic–Paleozoic in age. Titanite in a Natron amphibolite PH04-02 yields an age of 533 ± 7 Ma and an average ZiT temperature of ~760 °C (Table 2). Titanite in Arusha orthogneisses LJ04-26 and OM04-13 (Table 1) yields 528 ± 9 and

514 \pm 10 Ma dates, respectively, and a tight range of ZiT temperatures of 750–770 °C (Table 2). Dates for titanite grains in Arusha amphibolite LG04-37 range between 540 and 480 Ma (Fig. 7) and have average ZiT temperatures of ~770 °C (Table 2). Rutile in two Arusha schist and quartzite xenoliths (samples LG04-09 and LJ04-08) yields 500 ± 4 and 498 ± 3 Ma dates (Fig. 7) and both have overlapping 700–710 °C ZiR temperatures (Table 2). Apatite dates are highly variable among the Natron and Arusha mid-crustal xenoliths, but all are younger than coexisting titanite and rutile (Fig. 7); in Natron samples, apatite dates range from 515 to 470 Ma and in the Arusha samples 480–440 Ma (Table 2).

Accessory phase dates in granulite xenoliths are distinctive from those recorded in upper- and mid-crustal xenoliths. Zircon is only found in Natron mafic—intermediate granulite



Fig. 5 Labait apatite data. a Tera-Wasserberg concordia plot of apatite spot analyses from granite, schist, and amphibolite xenoliths. Most of the data fall along a 2.5-Ga reference isochron (see Table 2 for individual dates). Data are not common-Pb corrected. b, c Tera-Wasserberg plots of apatite spot analyses from two-pyroxene granulites. Both samples yield a spread of dates from 2.5 Ga to < 1 Ga with younger spots exhibiting higher LREE contents. Data are not common-Pb corrected. d, e Apatite depth profiles showing common-Pb corrected U-Pb date, LREE, and Sr core-rim variations. Rims are distinctly enriched in LREE and Sr contents, likely from melt interactions (see text for discussion). Lighter, thinner lines are individual profiles, and darker, bolder lines are averages of all profiles



xenoliths, is exclusively Archean (2.8–2.5 Ga), and has TiZ temperatures of 760–820 °C (Table 2). Titanite in one mafic Natron garnet granulite and two mafic Arusha garnet granulites yields Neoproterozoic–Mesozoic dates, which are discussed separately below. Granulite xenoliths in both the Natron and Arusha groups all contain near-zero rutile and apatite dates (Fig. 7; Table 2); in Natron granulites where quartz and zircon are present, ZiR temperatures are 690 and 770 °C (Table 2).

The presence of titanite overgrowths on rutile in the Natron and Arusha granulite xenoliths is given particular attention because they are retrogression features that can be linked to exhumation history of the lower crust (e.g., Manning and Bohlen 1991; Ernst and Liu 1998; Frost et al. 2001). Spot analyses of titanite in the two Arusha samples (Lashaine granulites 89–729 and 89–731) yield 550–260 Ma dates; depth profile data show a gradual decrease in age

toward the rims (Fig. 8d, e). Trace elements with distinct diffusivities—like Sr, Nd, Nb, and Zr (e.g., Holder et al. 2019)—show similar variability across the depth profiles in the two samples. By contrast, spot analyses of titanite in a Natron granulite (Kisite granulite KS04-10) vary between 550 and 440 Ma, but depth profiling does not show a rimcore relationship like that observed in the Natron granulites (Fig. 8d, f).

Discussion

Diffusive length-scales

To distinguish Pb loss by thermally mediated volume diffusion from non-diffusional processes (e.g., neocrystallization or recrystallization), we use the experimentally- and



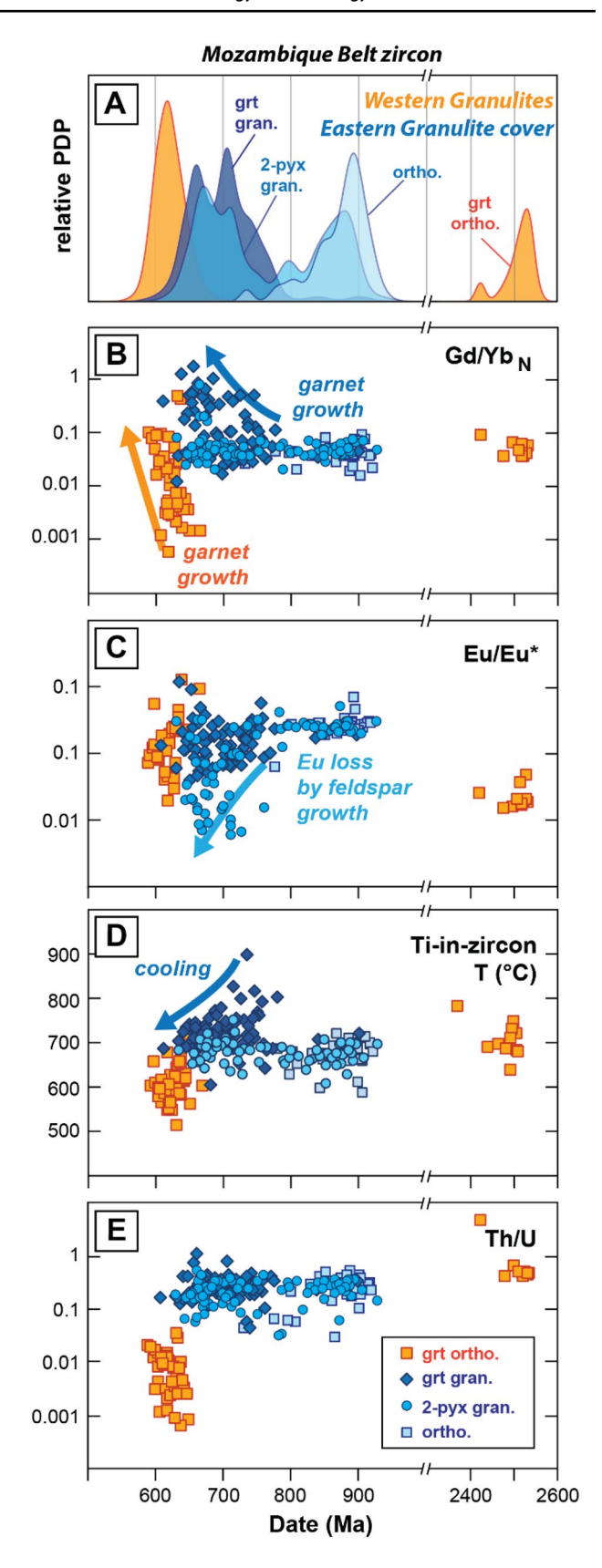
Fig. 6 Zircon from the Western Granulites and Eastern Granulite ► cover, Mozambique Belt. a PDPs of U–Pb dates. Zircon from the Western Granulites (orange) display a distinct bimodal distribution, with one Archean peak (2.6–2.4 Ga) and another Proterozoic peak (ca. 610 Ma). Zircon from the Eastern Granulites display a range of Proterozoic dates that differ among different sample types. Garnetabsent samples vary between 950 and 660 Ma, with prominent peaks at ca. 900 and 700 Ma, whereas garnet-bearing samples are largely centered between 800 and 660 Ma. b–e Trace-element and age variations. Note the distinct shifts in Gd/Yb, Eu/Eu*, and TiZ temperatures at ~770 Ma in garnet granulites from the Eastern Granulite cover. U–Pb date is the ²³⁸U/²⁰⁶Pb date < 1400 Ma and the ²⁰⁷Pb/²⁰⁶Pb date for > 1400 Ma

empirically derived diffusivities of multiple elements. We assess characteristic length scales assuming diffusion through a sphere, described by the following relationship (Crank 1975): $L = \sqrt{4Dt}$, where L is the characteristic diffusion length-scale, D is temperature-dependent diffusivity, and t is the duration of heating. If compositional variation in a mineral was driven by thermally mediated volume diffusion, elements with different diffusivities should record different length-scales for a given temperature and duration of heating (Fig. 9). Additionally, where volume diffusion is inferred, this simple relationship enables distinction between diffusion caused by thermal events separated by significant time intervals. In our study, this could be recent heating related to rifting (<4 Myr; Dawson 1992; Le Gall et al. 2008) versus long-term isothermal residence since orogeny (~600 Myr; Möller et al. 2000). Depth profiling is capable of resolving micron-scale near-rim variations—such as metamorphic rims or isotopic elemental gradients induced by thermally mediated volume diffusion (e.g., Cochrane et al. 2014; Smye and Stockli 2014; Stearns et al. 2016; Paul et al. 2019).

Multiple thermal imprints in the Tanzanian Craton

Archean thermal histories

Zircon, rutile, and apatite from Labait granite, schist, and amphibolite xenoliths indicate that the upper–middle crust of the craton has not experienced significant thermal overprinting since the Archean. Assuming that the upper and middle crust formed at similar times in the Archean, and integrating TiZ temperatures calculated for concordant zircon (~680 °C at ~2.68 Ga in amphibolites; Table 2) and the ages and the nominal Pb closure temperatures of rutile and apatite (2.6 and 2.5 Ga over ~550–400 °C), we calculate time-averaged cooling rates between 1 and 3 °C/Ma from 2.6 to 2.5 Ga (Table S4). The preservation of Neoarchean apatite dates further suggests that Proterozoic orogenies (Usagaran and East African), nor rifting has heated the upper–middle crust of the craton, even at its margin. Feldspar Pb isotope data from craton exposures near Dodoma (Fig. 1) do show





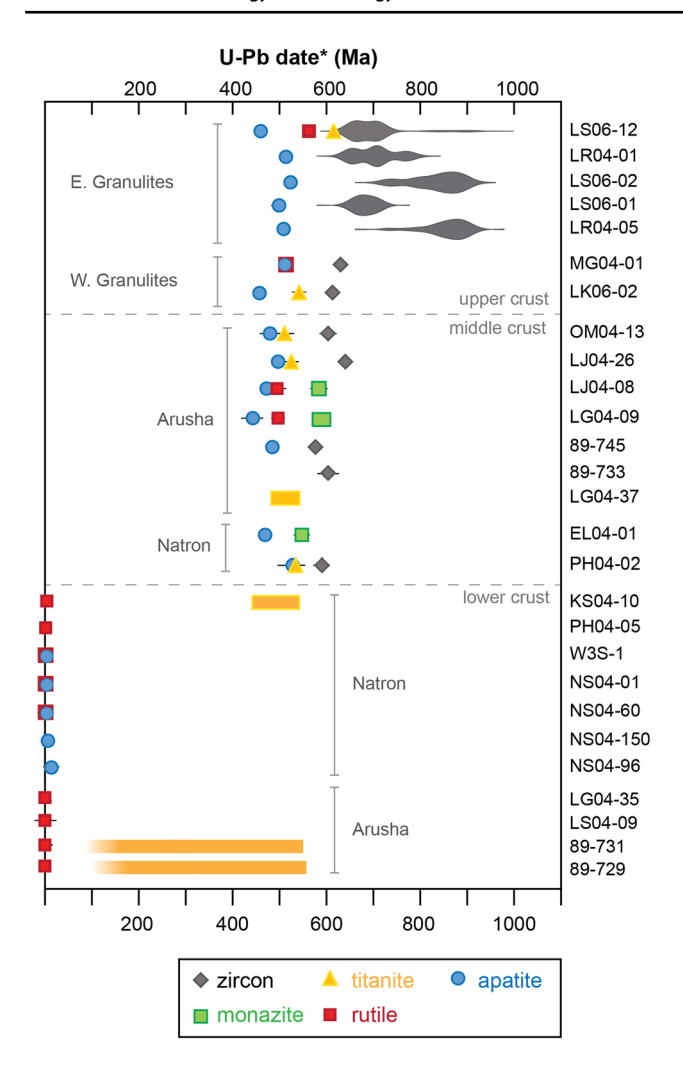


Fig. 7 Comparison of Proterozoic-Phanerozoic accessory phase U-Pb dates from xenoliths and surface outcrops from the East African Orogen. For zircon and monazite, only grains within 5% concordance are shown. All titanite, rutile, and apatite dates are common-Pb corrected (see Table S3 for common-Pb compositions). Bars represent ranges of dates. Gray blobs in Eastern Granulite cover zircon are PDPs. Concordia plots of each dated phase in the samples are presented in the Supplementary Materials

resetting at 2.0 Ga (Möller et al. 1998), suggesting that the Usagaran Orogen only impacted the southern portion of the craton and does not extend to the Labait region (Fritz et al. 2005).

In contrast to upper-middle crustal xenoliths, lower crustal granulite xenoliths from Labait show evidence for thermal pulses during later Archean, Neoproterozoic, and recent events. Neoarchean UHT conditions are recorded in TiZ temperatures of ≥950 °C at ca. 2.64 Ga in both the twopyroxene and garnet granulites (Fig. 3E). UHT conditions were likely accompanied by partial melting (e.g., Yakymchuk and Brown 2014) as indicated by the greater magnitude negative Eu anomalies in the hotter zircons (Fig. 3e). This trend reflects either buffered Eu³⁺/Eu²⁺ ratios during feldspar crystallization (Kohn and Kelly 2017) or changing redox state of the system (Hinton and Upton 1991). Although the Eu³⁺/Eu²⁺ ratio is redox-sensitive, this ratio is buffered by more dominant redox-sensitive elements (e.g., Fe), such that when feldspar removes Eu²⁺ during crystallization from a melt, some amount of Eu³⁺ is reduced to Eu²⁺ to maintain the Eu³⁺/Eu²⁺ ratio (Kohn and Kelly 2017). Because zircon preferentially incorporates Eu³⁺, zircon that co-crystallizes with feldspar will have increasing magnitudes of negative Eu anomalies over time at constant fO₂ conditions (Kohn and Kelly 2017). If the observed negative Eu anomalies were related to lower oxygen fugacity, one would expect Ce anomalies to become more subdued with date (Trail et al. 2012; Kohn and Kelly 2017), yet only a weak trend between Ce anomalies and date is observed (Fig. S7). The same trend could reflect protracted zircon growth from a melt; zircon is the only phase present that preferentially sequesters and depletes Ce⁴⁺ in the system (Trail et al. 2012). Zircon geochemical signatures are best explained by protracted zircon crystallization from a melt during Archean UHT metamorphism in the lower crust.

Ultra-high temperature metamorphism and partial melting of the lower crust of the Tanzanian Craton had previously been inferred on the basis of exsolved ternary feldspars in the two-pyroxene granulite xenoliths and significant whole-rock depletions of Cs, Rb, Th, and U (Mansur et al. 2014). Additional evidence for partial melting at this time is the presence of 2.66–2.62 Ga high-K granites on the craton (Maboko et al. 2006; Sanislav et al. 2014, 2018) as well as U-depletion inferred from Pb isotopes in feldspars from Western Granulites (Möller et al. 1998). Zircon temperatures are highest at 2.62–2.60 Ga in the granulite xenoliths, providing a temporal link between deep crustal metamorphism and granite production.

Neoproterozoic and Neogene heating

In addition to UHT metamorphism, the lower crust of the craton margin was affected by the East African Orogen and recent rifting. Previously, the only evidence for EAO-related events in the Labait lower crust was a garnet anorthosite containing plagioclase with Pb isotopic compositions plotting near a 550-Ma geochron (Mansur et al. 2014). Rutile in Labait garnet granulites dominantly yields Proterozoic and younger dates that point to a complex thermal history in response to the East African Orogen. While there is evidence of an Archean phase of rutile growth—two data points at ca. 2.5 Ga and ca. 1.1 Ga (inset in Fig. 4b)—it is difficult to draw conclusions based on so few data. The two older rutile spot analyses exhibit modest temperatures of ~750 °C (Fig. 4c), suggesting that the high ZiR temperatures recorded in the younger rutiles represent an additional high-temperature event after the Archean.



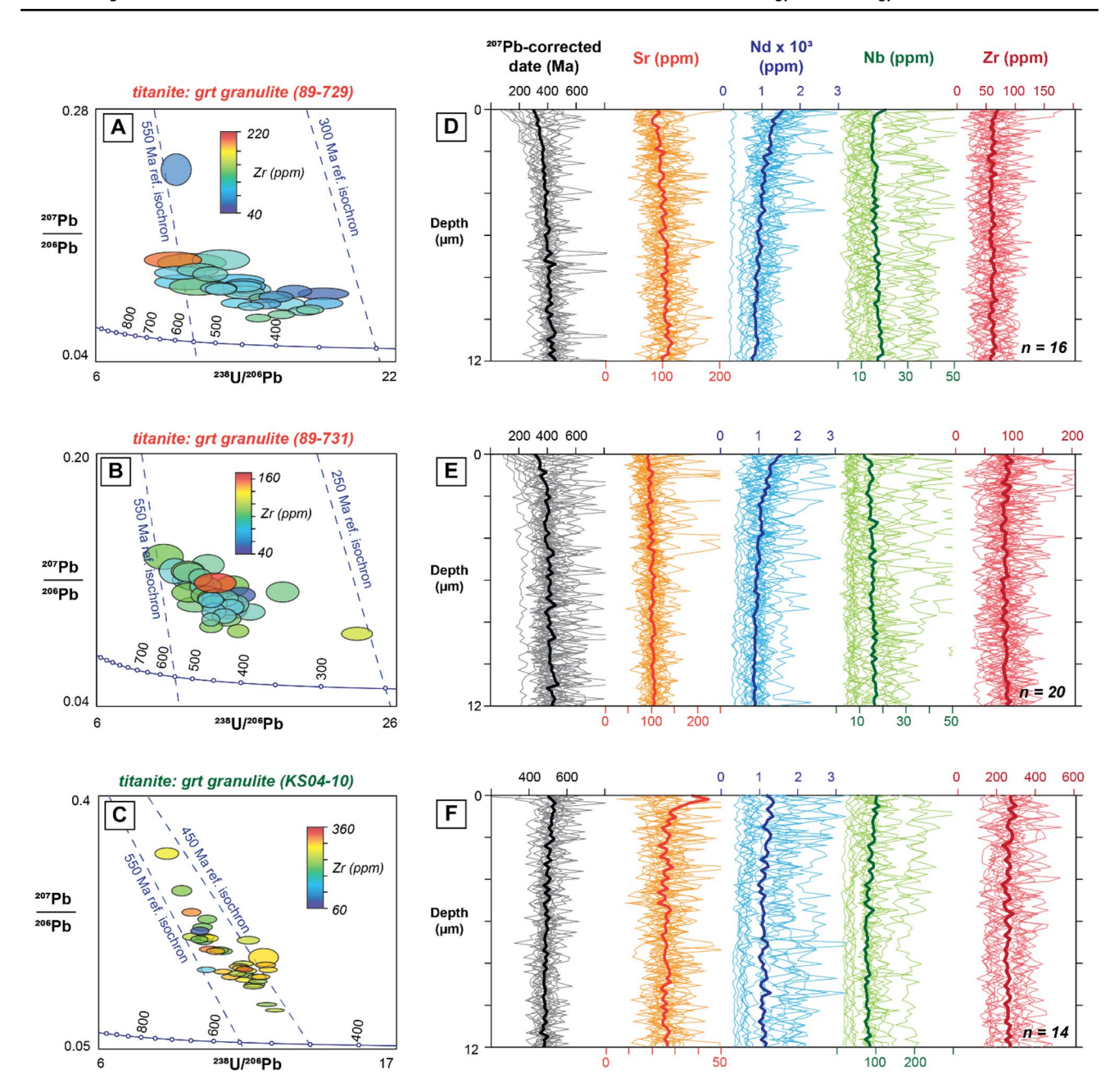


Fig. 8 Titanite data from lower-crustal xenoliths. a—c Spot analyses across titanite grains range from 550 to 250 Ma for the Lashaine granulites and 550 to 450 Ma for the Kisite granulite. See Table 2 for calculated ZiT temperatures. d, e Depth profiling of Lashaine whole titanite grains confirms the presence of young rims mantling cores. The selected trace-elements are ordered from faster to slower diffusing from left to right (after Cherniak 1995; Kohn 2017; Holder et al. 2019). The topologies of the different elements vary over similar

length scales, contrary to variable topologies that would be produced by thermally mediated volume diffusion. Instead, age and elemental variations could reflect mixing of a thin young rim with an older core, similar to what was observed in the metasomatised Labait apatite. f Depth profiles of Kisite titanites. Note how unlike the Lashaine titanites, these titanites have generally uniform compositions with depth. A general decrease in age with depth in these titanites reflects higher proportion of common-Pb at the grain surface

Indeed, the most concordant rutile data at 600–500 Ma record elevated ZiR temperatures of ~820 °C, which implicate the EAO (Fig. 4d). Most ZiR temperatures, however, do not correlate with date (Fig. 4d). Recrystallization and Pb loss during post-orogenic cooling and/or rift-related

heating may explain the disparate U-Pb and trace-element patterns.

The range of ZiR temperatures may represent diffusive resetting, distinct thermal events, or variable $aSiO_2$ and/or $aZrSiO_4$ during rutile crystallization. The combined data



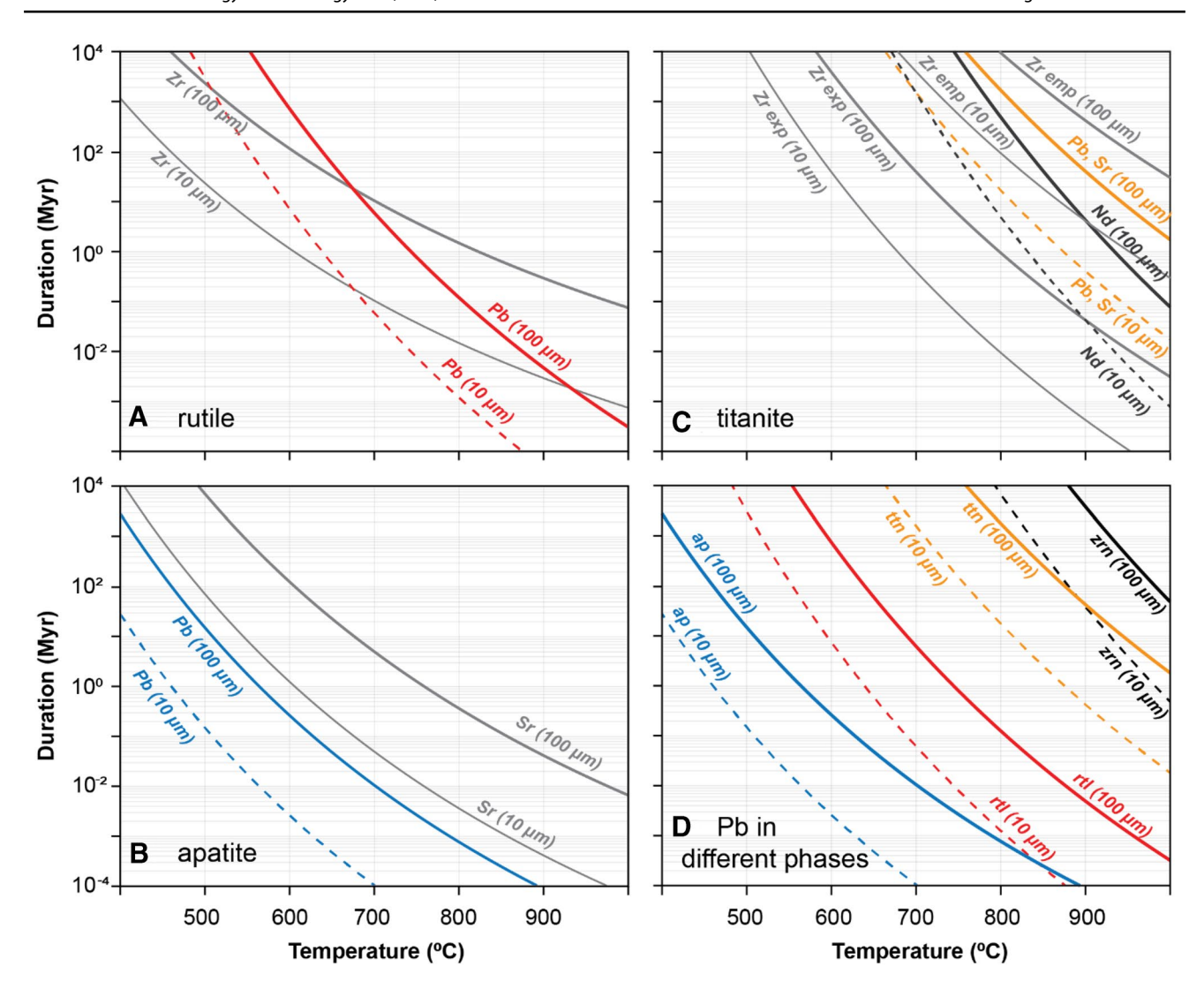


Fig. 9 Characteristic length-scales of diffusion for different elements in different phases across relevant temperatures and durations. Length-scales of key elements would be expected to vary by orders magnitude were thermally mediated volume diffusion at play. a Comparing Zr and Pb length-scales for rutile. Diffusivity data for Zr from Cherniak (2006) and Pb from Cherniak (1993). b Comparing Sr and Pb length-scales for apatite. Diffusivity data for Sr and Pb from Cherniak et al. (1991). c Comparing Zr, Nd, Sr, and Pb length-scales for

titanite. Diffusivity data Nd from Cherniak (1995) and Sr and Pb from Kohn (2017) and Holder et al. (2019). Experimental Zr diffusivity data from Cherniak (2006) (Zr exp) and empirical Zr diffusivity data from Holder et al. (2019) (Zr emp). **d** Comparing characteristic length-scales of diffusion for Pb in different phases. Diffusivity data for rutile, apatite, and titanite same as other panels. Zircon Pb diffusivity data from Cherniak (2010)

suggest that variable aZrSiO4 is the most likely scenario. The spread of ZiR temperatures is not likely to be related entirely to diffusive loss of Zr during rift-related heating. For 4 Myr at holding temperatures of 800 °C (oldest rift magmatism in the area; Dawson 1992), Zr diffusion would occur over length-scales of ~ 120 μ m and the U–Pb system would be reset across the whole rutile grain (> 200 μ m; Fig. 9a) (Ewing et al. 2013; Pape et al. 2016), contrary to the preservation of Mesoproterozoic and older dates. Given the lack of any trend between ZiR temperature and U–Pb dates (Fig. 4d), it is also difficult to argue that the range of ZiR temperatures reflects mechanical mixing

between discrete domains during ablation. By contrast, the absence of EAO-age zircon in all of the Labait granulite xenoliths is evidence that $aZrSiO_4$ was not unity during Proterozoic rutile crystallization, and consequently, the range of ZiR temperatures may reflect variable $aZrSiO_4$ (plus $aSiO_2$). Several studies have observed that ZiR temperatures in high-grade rocks are highly variable and have posited that maximum ZiR temperatures closely approximate peak temperatures (e.g., Kooijman et al. 2012; Kohn et al. 2016; Zack and Kooijman 2018; Clark et al. 2019). The simplest explanation for our data is that rutile (re)



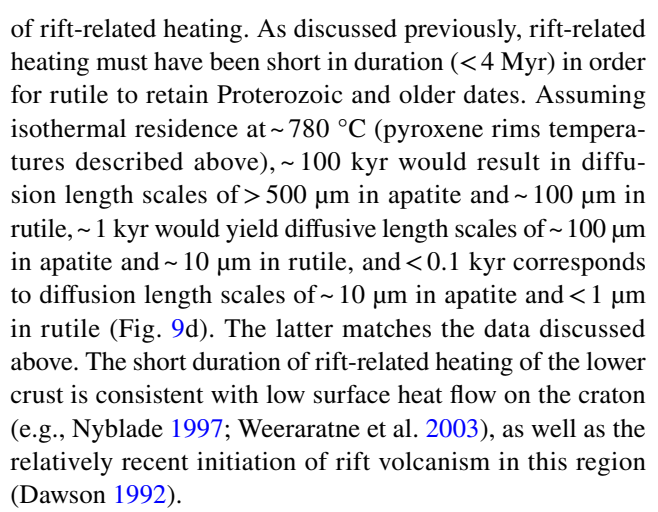
crystallized during the EAO with variable aZiSiO₄ and/or aSiO₂ and underwent subsequent partial Pb loss.

Partial Pb loss in the rutile likely occurred during prolonged residence at elevated temperatures after the EAO. Characteristic diffusion length scales derived from Pb diffusivities (Cherniak 2000; Smye et al. 2018) for 600 Myr of isothermal residence are ~4 µm at 500 °C, ~20 µm at 550 °C, and 80–86 µm at 600 °C, consistent with the preservation of Mesoproterozoic dates observed in the analyzed rutile grains (Fig. 9a). Thus we suggest that for most of its history, the cratonic lower crust remained at 500-600 °C—temperatures hot enough for partial Pb loss, but cool enough to avoid complete rutile resetting.

In addition to EAO-related metamorphism, there is evidence for rift-related overprinting of the deep crust from apatite in two-pyroxene granulites (Fig. 5). CL-dark patches occur close to grain rims and along cracks and resemble fluid infiltration textures (e.g., Harlov et al. 2005). Depth profiles show that these are young domains with elevated Sr and LREE-enriched signatures that overprint homogeneous, older cores—2.3-1.8 Ga in sample LB04-36 and ca. 400 Ma in sample LB04-86 (Fig. 5d, e). These older core dates likely correspond to original cooling times. Notably, U-Pb dates, Sr, and LREE contents vary over similar length scales (~2-3 µm), indicating they do not solely reflect element mobility by thermally mediated volume diffusion (Fig. 9b).

Rift-related overprinting in Labait granulite xenoliths was suggested by Mansur et al. (2014) based on pyroxene rims that recorded elevated temperatures (~780 °C). Additionally, grain-boundary alteration around plagioclase in an anorthosite xenolith has Pb isotopic ratios that lie along a present-day geochron (Bellucci et al. 2011). The young ages of Labait apatite rims further implicates a rift-related process. This overprinting, which is associated with elevated LREE contents, may be due to carbonatite melt interactions. Similar LREE enrichments have been observed along grainboundaries in other Tanzanian xenoliths, including Lashaine garnet granulites (Mansur et al. 2014; this study) and peridotites (Ridley and Dawson 1975), and in clinopyroxene dunite xenoliths from Olmani (Rudnick et al. 1993), where carbonatitic melts have extensively altered portions of the mantle lithosphere. We speculate that these low-viscosity, low-degree partial melts intruded along grain boundaries within the lower crust in response to rifting and generated the metasomatized domains observed in the apatite.

Although heating and fluid infiltration associated with rifting has affected the deep crust of the craton—as evidenced by textures and dates of apatites and pyroxene rims in some two-pyroxene granulites—it has not yet erased earlier metamorphic/thermal histories. The preservation of older Archean-Proterozoic dates in rutile and apatite in granulite xenoliths imposes key constraints on the duration



Contributions to Mineralogy and Petrology

Finally, the post-Archean thermal history inferred from rutile and apatite analyses of granulite xenoliths appears, at first glance, to conflict with previously reported feldspar Pb isotopic data, which suggested that the lower crust of the craton remained cool (below 600 °C—the closure temperature for Pb diffusion in feldspar) since the Archean (Bellucci et al. 2011). The discrepancies between the inferred thermal histories can be reconciled if feldspar did not undergo isotopic exchange with high U/Pb phases—like apatiteduring post-Archean thermal events, yet temperatures were high enough to enable such Pb exchange. Thus, the fact that feldspar only exhibits Archean Pb isotopic signatures may either reflect the short duration of later heating, or that post-Archean isotopic signatures were not captured by previous in situ methods, which focused on the grain interiors away from rims where overprinting would be first recorded (Bellucci et al. 2011).

Thermal evolution of the East African Orogen

Neoproterozoic metamorphism and post-orogenic cooling of the Eastern and Western Granulites

Granulites exist at the surface of the East African Orogen and as xenoliths from the underlying lower plate (Fig. 1). Petrochronological analyses of the Eastern Granulite cover and the Western Granulites enable distinction from granulite xenoliths. Additionally, when combined with previously published dates (Möller et al. 2000), the data offer insight into the tectonic and thermal history of the orogen.

Samples from the Eastern Granulite cover record protracted zircon growth from 915 to 630 Ma and lack any Archean inheritance (Fig. 5a; Möller et al. 1998; Sommer et al. 2005; Hauzenberger et al. 2007; Tenczer et al. 2006, 2013). The range of zircon dates in these rocks overlap with arc rocks elsewhere in the orogen (Fritz et al. 2013) and support previous suggestions that the Eastern Granulites cover and basement is derived from an outboard arc terrane that



was accreted onto Africa during the EAO (e.g., Appel et al. 1998; Möller et al. 2000). TiZ temperatures in garnet granulites record crystallization from ~830 °C at 780–700 Ma to ~640 °C at 640 Ma (Fig. 6d) along a retrograde cooling path (e.g., Kelsey and Powell 2011; Kohn 2017). Initial garnet growth, as recorded by elevated Gd/Yb_N ratios in zircon at 780–760 Ma (Fig. 6b), occurred shortly before the onset of cooling. Growth of clinopyroxene over garnet, like those observed in our samples (Fig. S1) was interpreted as evidence of isobaric cooling of the Eastern Granulites (e.g., Appel et al. 1998), and the zircon temperature trends may record part of this cooling period.

The Western and Eastern Granulites underwent multiple episodes of metamorphism during the East African Orogeny (e.g., Stern 1994; Meert 2003; Fritz et al. 2009). The youngest zircon and monazite U-Pb dates from the Eastern Granulites are 645-630 Ma (Möller et al. 2000; Tenczer et al. 2013; this study) and have been interpreted to date metamorphism during later magmatic underplating (Appel et al. 1998; Möller et al. 2000). Neoproterozoic zircon rims from the Western Granulites (630-615 Ma; Sommer et al. 2003; Cutten et al. 2006; this study) are younger than those from the Eastern Granulite cover, but older than the onset of continent-continent collision (560-550 Ma; Fritz et al. 2013). Similarly, metamorphic titanite dates in the Eastern Granulites (620–610 Ma; Möller et al. 2000; this study) are coincident with the Western Granulite zircon dates, indicating that metamorphism occurred in both terranes prior to 560-550 Ma collision. Meert (2003) proposed at least two collisional events during the assembly of Gondwana: one ca. 630-610 Ma, representing the timing of accretion of outboard arc terranes and continental blocks onto West Gondwana/East Africa, and another 570-530 Ma marking collision between the newly amalgamated West Gondwana terranes with East Gondwana. Consequently, 630-610 Ma metamorphic zircon and titanite dates record metamorphism during emplacement of the Eastern Granulite basement/ cover onto the East African margin.

Rutile and apatite in the Western and Eastern Granulites record cooling following the collisional events discussed above. Cooling rates are calculated using the U–Pb dates of two or more phases in a sample and their respective Pb closure temperatures. In the Western Granulites, 545 Ma titanite dates (this study) and 560–540 Ma metamorphic zircon and monazite dates (Le Goff et al. 2010; Tenczer et al. 2013) document metamorphism during continental collision. This was followed by cooling through rutile Pb closure at ~515 Ma and apatite Pb closure at ~510 Ma and ~460 Ma (Table 2), yielding time-averaged cooling rates of 4–30 °C/Myr from 540–510 Ma (assuming cooling from ~775 °C; Table S4). The Loibor Serrit Eastern Granulite cover samples record cooling after accretion at 620–610 Ma (titanite data; Möller et al. 1998; this study); these rocks cooled

through rutile closure ca. 560 Ma and apatite closure from 520–460 Ma, or at a rate of 1–6 °C/Myr from 620 to 460 Ma. Similar cooling rates were determined using integrated U–Pb TIMS dating of zircon, monazite, titanite, and rutile and K–Ar and Ar–Ar dating of hornblende, biotite, muscovite, and K-feldspar of gneisses from the Eastern Granulite basement along strike in eastern Tanzania (Maboko et al. 1989; Möller et al. 2000).

Post-collisional cooling history of the middle-lower crust

Mid-crustal xenoliths record cooling rates similar to those of outcrops. Some mid-crustal xenoliths have 640-545 Ma monazite and zircon dates that suggest metamorphism during the EAO (Fig. 7; Table 2). Titanites in Natron and Arusha orthogneiss and amphibolite xenoliths are ca. 530 Ma and 540–480 Ma, respectively (Table 2). These dates are generally younger than those in either the Western or Eastern Granulites (Table 2; Möller et al. 2000) and do not appear to correspond to any discrete tectonic event in the area. The titanite dates could reflect growth after peak metamorphism or resetting by some later processes (e.g., fluid interactions; Spencer et al. 2013), but are probably not cooling dates as they crystallized below the nominal > 800 °C titanite Pb closure temperature (Table 2). Rutile and apatite dates (Fig. 7) are 520-470 Ma for the Natron xenoliths and 500-440 Ma for the Arusha xenoliths, and are interpreted to constrain cooling from 550 to 400 °C (e.g., Smye et al. 2018). Cooling rates of mid-crustal xenoliths are 2-7 °C/Myr for the Natron and 1–3 °C/Myr for the Arusha xenoliths from ~550 to 440 Ma (Table S4). Both rates are similar to one another and are within the range of cooling rates calculated for the upper crust in this study.

Accessory phases from Natron and Arusha lower crustal garnet granulite xenoliths have U–Pb dates distinct from those from the upper and in middle crustal xenoliths (Fig. 7). Zircon is exclusively Archean, but rutile, apatite, and titanite in these lower crustal xenoliths are significantly younger than those at higher crustal levels. These data provide insight into the post-collisional cooling history of the lower crust of the EAO.

Peak metamorphic pressures for lower crustal xenoliths from the Natron and Arusha areas are up to 2.0 GPa during the EAO (Mansur et al. 2014; this study). Because the crust is ~40 km-thick today (Julià et al. 2005), the crust as a whole has undergone significant thinning or exhumation since orogeny. Near-zero age rutile and apatite from the granulite xenoliths (Fig. 7) preclude determining a specific exhumation/cooling history for the lower crust: these dates could reflect protracted residence above closure temperatures (600–700 °C) or recent heating by rift magmas (> 800 °C) (see previous discussion).



In contrast to rutile and apatite, titanites in Lashaine and Kisite garnet granulite xenoliths capture the post-collisional thermal history of the lower crust, with titanite overgrowths on rutile (Fig. 10) tracking the retrograde path (e.g., Manning and Bohlen 1991; Ernst and Liu 1998; Kohn 2017). Pseudosection modeling of garnet granulite xenoliths derived from the lowermost crust (samples 89–729 and 89–731)—with sample 89–729 shown for reference in Fig. 10—places the rutile-titanite transition between 1.0 and 1.6 GPa at 550–850 °C. The high-pressure stability of

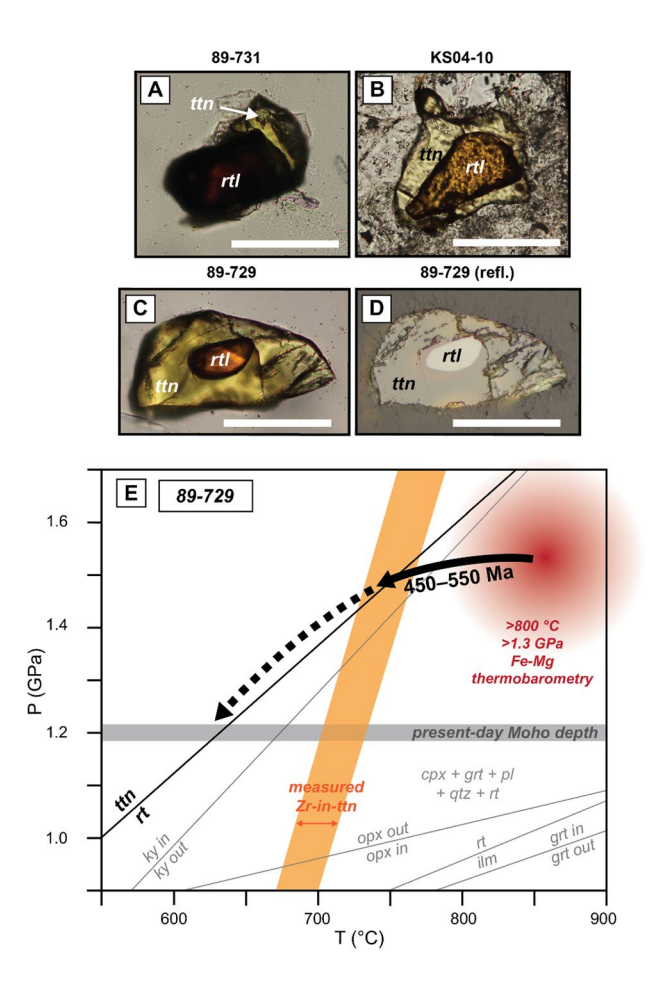
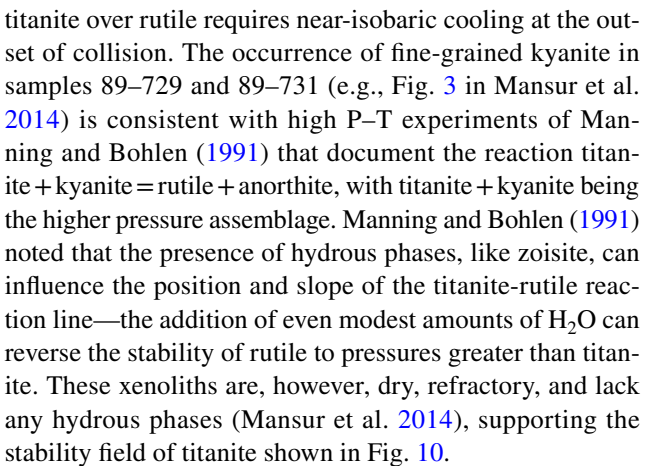


Fig. 10 Constraints on P-T evolution of the lower crust from titaniterutile pairs in granulite xenoliths. a-d Rutile core in titanites from the Lashaine and Kisite granulite xenoliths indicate titanite growth during cooling and decompression after peak metamorphism. White bars are ~ 100 µm wide. e Phase diagram for Lashaine granulite 89–729 (taken to be representative for all the granulites). The titanite-rutile phase boundary is from pseudosection modeling conducted in this study (see Supplementary Materials). Orange bars represent constraints from ZiT thermometry for 89-729 titanite (similar to titanite from the other samples) using $aSiO_2 = 0.5$ as a minimum bound, (Ferry and Watson, 2007). Zr contents in titanite suggest formation during cooling after peak metamorphism (red circle; P-T constraints from Mansur et al. 2014). Dashed arrow represents a possible P-T path from peak conditions, through the titanite-rutile boundary, and to pressures corresponding to the present-day Moho (horizontal grey bar)



ZiT thermometry constrains the retrograde P–T path into the titanite stability field, and the magnitude of cooling depends on the $a\mathrm{SiO}_2$ and $a\mathrm{ZrSiO}_4$ used to calculate apparent titanite temperatures. Granulites 89–729 and 89–731 lack quartz, so $a\mathrm{SiO}_2$ is certainly less than 1. Using $a\mathrm{SiO}_2=0.5$ as a minimum bound—based on the presence of feldspars instead of feldspathoids (Ferry and Watson 2007)—a possible cooling path from 840 °C (peak temperatures from Mansur et al. 2014) to \leq 750 °C is inferred (intersection of ZiT apparent temperatures at the titanite-rutile phase boundary; solid black arrow in Fig. 10). Further cooling and decompression towards 1.2 GPa (i.e., the present-day Moho) is inferred for the lower crust (dashed black arrow in Fig. 10).

Titanite U–Pb dates provide constraints on the timing and rate of lower crust cooling. Spot analyses and depth profiles of lower crustal titanites yield dates as old as 560 Ma (taken as growth following peak metamorphism in the EAO) and extend to Paleozoic and younger dates: < 100 Ma in depth profiles through titanites in granulites 89–729 and 89–731 (Fig. 8a–d), to as young as 440 Ma in granulite KS04-10 (Fig. 8e, f). The spread to younger dates likely relate to the cooling history and may reflect the following: (1) Pb diffusion from the grain during residence at elevated temperatures; (2) protracted titanite growth during cooling; (3) partial resetting by fluids, melts, etc. during post-orogenic exhumation; or (4) mechanical mixing with a thin, young rim during laser ablation. Each of these possibilities is considered in turn.

Diffusional Pb loss can be eliminated based on depth profiles through the titanites. Titanites in Arusha samples 89–729 and 89–731 reveal monotonically decreasing dates toward the grain rims that co-vary with multiple trace elements. Although the U–Pb profiles appear to follow a topology resembling diffusive Pb loss (Fig. 8b, d), elements with different diffusivities—like Sr, Nd, and Zr (Cherniak 1995, 2006; Kohn 2017; Holder et al. 2019)—vary in concentrations over similar distances, contrary to the pattern predicted by thermally mediated volume diffusion (Fig. 9c; see also discussion in Stearns et al. 2016). For example, using



experimental diffusivity data from Cherniak (2006), length scales of Zr for ~ 100 Myr residence at ~ 700 °C are expected to be an order of magnitude greater than for Pb, Sr, and Nd (Fig. 9c). However, using empirical Zr diffusivity data (Holder et al. 2019), length scales of Zr are $< 2 \mu m$ at the same conditions (Fig. 9c), and could be even shorter (Stearns et al. 2016). Titanite Nd and Zr profiles do not show significant outward diffusion (Fig. 8d, e), suggesting that postorogenic residence temperatures were < 700 °C, well below Pb closure in titanite (Kohn 2017). Additionally, maximum ZiT temperatures (assuming that $aSiO_2 = 1$) are 780–810 °C at ~ 1.6 GPa (Fig. 10), which lie at the lower end of the proposed range of titanite Pb closure temperatures (> 800 °C; using titanite Pb diffusivities reported in Kohn 2017). Thus, the titanites did not undergo significant Pb diffusion during slow cooling following the EAO, and the younger Paleozoic titanite dates reflect process 2, 3 or 4 listed above.

Protracted titanite growth during cooling is also unlikely. Were this the case, titanite dates would be expected to correlate with ZiT temperatures, but they do not (Fig. 8). Isothermal titanite growth for > 300 Myr in the lower crust is also improbable because the upper and middle crust had undergone significant cooling and exhumation from 560–460 Ma (Table 2). The variable titanites dates thus correspond to resetting by non-diffusional processes and/or mixed sampling of discrete age domains.

Several studies have suggested that titanite can be reset via fluid infiltration during retrogression (Frost et al. 2001; Bonamici et al. 2015; Garber et al. 2017; Marsh and Smye 2017; Walters and Kohn 2017; Holder and Hacker 2019). The outermost 5 µm of titanites from the Lashaine mafic garnet granulites have trace-element patterns that are consistent with growth from a near-homogeneous medium along grain boundaries (fluid or melt). Alteration along grain boundaries in Lashaine garnet granulites is LREE-enriched and Pb isotopes suggest this alteration occurred very recently (Mansur et al. 2014), implicating the influence of rift-related metasomatism. High-resolution X-ray mapping using wave-length dispersive spectroscopy (WDS) documents the presence of variable thickness (3–30 µm) titanite rims enriched in Nd and Ce relative to the grain interior (Fig. S20). We conclude that the 550–250 Ma titanite spot analyses (Fig. 8)—like the < 10 Ma, LREE-enriched rims of Labait apatite—are the result of mixing between an older Proterozoic core with a rim that formed during the Cenozoic, likely during riftrelated metasomatism (i.e., processes 3 and 4 listed above). Titanite in garnet granulite xenolith KS04-10 from the Natron region has U-Pb dates that range from 550-440 Ma (Fig. 8c, f), but does not exhibit near-rim variations like those observed in the Lashaine granulites; this sample, therefore, eluded rift-related metasomatism and preserves the original data range associated with cooling and exhumation of the lower crust.

In sum, titanite petrochronology suggests that the lower crust cooled from > 840 °C to temperatures as low as 750 °C shortly after the EAO (as early as 560 Ma), followed by prolonged cooling (~0.2 °C/Myr) and decompression to the present-day Moho. Because diffusional Pb loss is not observed in the titanites, we infer that the lower crust has remained well below the Pb closure temperature of titanite since the Proterozoic. Recent growth of titanite rims associated with rift-related metasomatism of the lower crust in the Arusha region resulted in apparent titanite dates down to ~ 100 Ma. Finally, the absence of radiogenic Pb in rutile and apatite in lower crustal xenoliths implies residence above the Pb closure temperatures of these phases, corresponding to presentday lower crustal temperatures of > 650 °C (total radiogenic Pb loss in rutile; Kooijman et al. 2010) and < 750 °C (ZiT temperatures; Fig. 11).

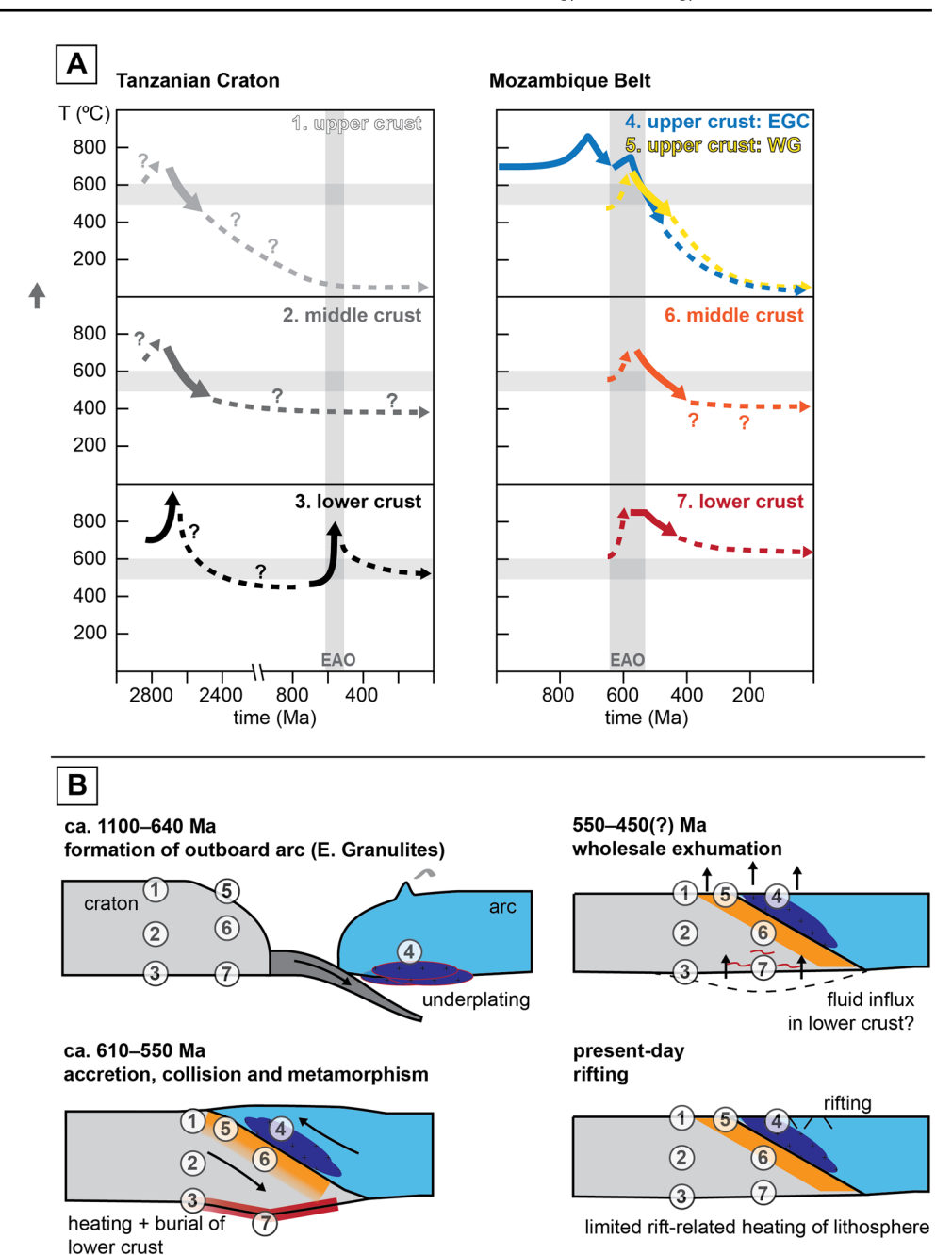
Variable present-day thermal structure of the lithosphere

The data discussed above provide constraints on the present-day thermal structure of the lithosphere. Surface heat flow in the East African Orogen is higher than on the craton (average $47 \pm 8 \text{ mW/m}^2$ for the orogen versus $38 \pm 8 \text{ mW/m}$ m^2 [all ± 1SD] at the craton margin; Nyblade 1997), reflecting greater crustal heat production and/or mantle heat flow beneath the orogen. Crustal heat production is probably not much greater in the orogen given the scarcity of heat-producing element enriched plutons (e.g., Appel et al. 1998; Fritz et al. 2005) and the presence of refractory, Archeanaged crust beneath the orogen (Mansur et al. 2014). Hotter Moho temperatures—derived from residence temperatures of garnet granulite xenoliths—for the orogen compared to the Tanzanian Craton (650-750 °C vs. 500-600 °C, respectively) also suggest greater heat input from the underlying mantle and may be a consequence of the greater intensity of rift-related heating below the orogen.

To gain first-order insight into the potential causes of variable mantle heat flow across NE Tanzania, we calculate 1-D steady state geotherms assuming conductive heat flow through the lithosphere and an exponential decrease in heat production with depth (Fig. 12; see Supplementary Materials for details of calculations and model parameters). We do not incorporate the effects of depth-dependent thinning of the lithosphere. Inferred Moho temperatures for the craton margin at Labait are 500-600 °C and fall between 40 and 50 mW/m² geotherms (Fig. 12), typical of cratons elsewhere (e.g., Rudnick et al. 1998; Hasterok and Chapman 2011). Higher temperatures of 650–750 °C inferred for the lower crust of the orogen correspond to higher geotherms of 50-60 mW/m² (Fig. 12), similar to other Proterozoic orogens (e.g., Jaupart and Mareschal 2014). Importantly, the geotherms that encompass the range of orogenic Moho temperatures



Fig. 11 a Schematic diagram illustrating cooling rates of the different crustal levels of the Tanzanian Craton and Mozambique Belt. Solid lines represent cooling paths constrained by petrochronology, whereas dashed lines represent inferred cooling paths (with question marks indicating highly uncertain paths). From the craton. Labait granite xenoliths are taken as representative of the upper crust, schist and amphibolite xenoliths as sampling the middle crust, and granulite xenoliths from the lower crust. From the Mozambique Belt, outcrops are taken as upper crustal samples, amphibolite and orthogneiss xenoliths from the middle crust, and granulite xenoliths from lower crust. The upper crust of the craton appears to record Archean cooling, whereas the lower crust underwent heating during the EAO and recently during rifting (not shown). In contrast to the craton, the entire crust of the Mozambique Belt underwent relatively rapid cooling following the EAO, with differences in the post-collisional thermal histories relating to later melt/ fluid metasomatism during later slow cooling (also not shown). The horizontal gray bar represents the nominal range of Pb closure temperatures for rutile and apatite; above this bar, both phases are open to total Pb loss, and below it, both phases retain radiogenic Pb. b Cartoon showing tectonic interpretations. Numbered circles correspond to numbers in panel a



intersect the mantle adiabat at shallower depths, indicating a thinner mantle lithosphere below the orogen (< 120 km lithospheric thickness, but it could be thinner if crustal heat production is lower than what we assume). This inference is also supported by Rayleigh wave tomography (~100 km lithosphere thickness; Weeraratne et al. 2003) and the general scarcity of garnet-bearing mantle lithologies throughout the Mozambique Belt (Cohen et al. 1984; Dawson and Smith 1988; Rudnick et al. 1994; Lee and Rudnick 1999; Aulbach et al. 2011).

A thinner mantle lithosphere below the orogen is the likely cause of increased mantle heat flow beneath the orogen compared to the craton margin. However, whether greater mantle heat flow reflects an intrinsically thinner mantle lithosphere or a lithosphere thinned by rifting is unclear. Most mantle xenoliths from the Mozambique Belt are refractory and ancient (Rudnick et al. 1994; Burton et al. 2000)—though many have also undergone later metasomatism—suggesting the mantle keel is still relatively intact (e.g., Rudnick et al. 1994; Aulbach et al. 2011). Additionally, although some crustal xenoliths from the orogen record recent reheating (Jones et al. 1983; Mansur et al. 2014), the petrochronological data presented here do not require additional advective heat sources to explain lower-crustal



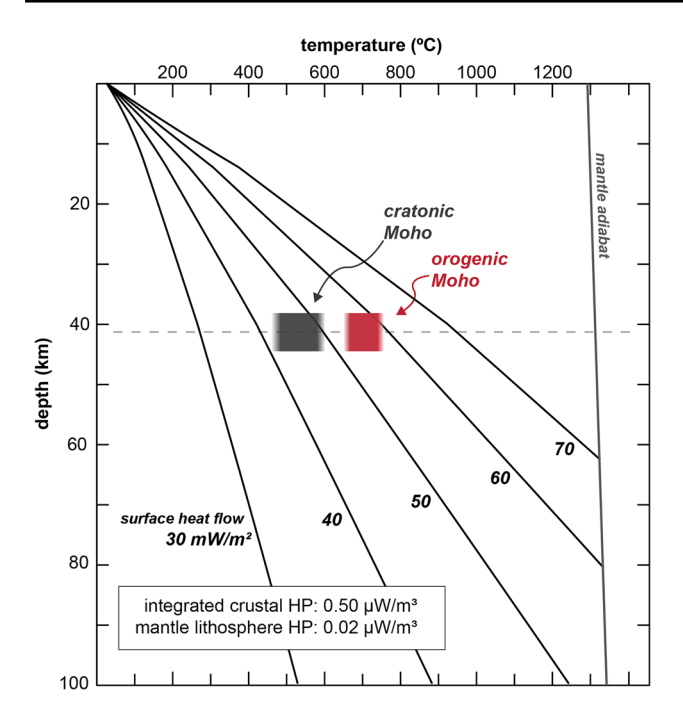


Fig. 12 Comparison of inferred Moho temperatures for the craton margin (Labait; gray) and the EAO (Lashaine; red) with modeled geotherms. Bar widths represent the inferred temperature range for the lowermost crust, assumed to be Moho temperatures. All the geotherms are modeled by assuming purely conductive heat flow through the lithosphere and employ the same lithospheric heat production (HP) profile (Furlong and Chapman 2013); only mantle heat flow—and hence surface heat flow—is varied. See Supplementary Materials for specific model parameters

temperatures of 650–750 °C for the orogen. Thus, if thinning due to recent rifting has occurred, it has been relatively minor and has not resulted in catastrophic removal of the mantle lithosphere below the EAO.

Conclusions

New multi-phase U-Pb and trace element data from cross sections through the crust provided by outcrops and deep crustal xenoliths elucidate the thermal histories of the Archean Tanzanian Craton and adjacent East African Orogen. The data suggest the following:

• The upper-middle crust of the Tanzanian Craton margin (Labait) has eluded major thermal perturbations during the Neoproterozoic East African Orogeny and Cenozoic rifting. In contrast, the lower crust of the craton margin experienced Neoarchean UHT metamorphism/ melting, EAO-related heating, post-orogenic slow cooling and rift-related fluid/melt interactions. The retention of older age domains in rutile, apatite, and feldspars in lower crustal granulite xenoliths (Bellucci et al. 2011;

- this study) suggest minimal reheating by rifting (at most 0.1 kyr of heating assuming \sim 780 °C) and residence at 500–600 °C prior to eruption
- Metamorphism of the Eastern and Western Granulites occurred ca. 630-610 Ma (zircon and titanite dates) during accretion of the Eastern Granulites onto the East African margin (Meert 2003) (Fig. 11). At the time of collision ca. 560-550 Ma, the Eastern Granulite basement and cover had cooled below rutile closure (Möller et al. 2000; this study), but the Western Granulites did not cool below rutile closure until ca. 515 Ma. By ca. 450 Ma, both the Eastern and Western Granulites had cooled below apatite closure (Fig. 11), consistent with the thermal histories constrained by K-Ar and Ar-Ar hornblende, biotite, muscovite, and K-feldspar dates (e.g., Maboko et al. 1989; Möller et al. 2000). Rutile and apatite dates from mid-crustal xenoliths erupted through the orogen overlaps those from outcrops, indicating similar cooling histories.
- Lower crustal xenoliths from the orogen at the Natron and Arusha sites record post-collisional thermal histories. Titanite U–Pb dates document cooling from over 800 °C to ~750 °C by 550 Ma, followed by slower exhumation to present-day crustal thickness of ~40 km (Fig. 10). Near-zero age rutile and apatite suggest that the lower crust resided above the Pb closure temperatures of rutile and apatite during post-collisional cooling, or that these minerals were reset by recent rift-related heating. The absence of thermally mediated volume diffusion in titanite suggests minimal perturbation by heating and that pre-eruptive residence temperatures were below 750 °C. Near-zero age rutile and apatite indicate residence above 650 °C and need not reflect recent reheating.
- Lower-crustal temperatures for the East African Orogen are higher than inferred for the Tanzanian Craton (650–750 °C vs. 500–600 °C, respectively), consistent with the higher surface heat flow observed for the orogen (Nyblade et al. 1990; Nyblade 1997). Data from the orogen suggest a hotter geotherm compared to the craton and are compatible with increased mantle heat flow as a result of a thinner mantle lithosphere (e.g., Rudnick et al. 1994; Lee and Rudnick 1999; Weeraratne et al. 2003; Aulbach et al. 2011). Conductive heat transfer through a thinner mantle lithosphere can explain the data without additional advective heat sources, suggesting that rifting has had only a limited impact on the thermal structure of the crust and did not result in significant removal of the mantle keel.

Acknowledgements This work is dedicated to the memory of our dear friend T. Alex Johnson (1991–2020). Funded by National Science Foundation (NSF) Grants EAR-0337255 awarded to R.L. Rudnick,



EAR-1650260 awarded to R.L. Rudnick and J.M. Cottle, a Grant from the National Geographic Society (7836-05) to R.L. Rudnick, and an NSF graduate research fellowship to F.E. Apen. The Tanzanian Commission of Science and Technology supplied the necessary research permits to collect the samples. Sean Timpa, Shukrani Manya, Adam Mansur and Dusty Aeiker are thanked for assistance in the field; Sean Timpa and Adam Mansur helped with initial sample processing. We also thank Bradley Hacker, Joshua Garber, and Alex Johnson for enlightening discussions, and Khalil Droubi for assistance with sample preparation and mineral separations. We gratefully acknowledge Othmar Müntener for editorial handling and Andreas Möller, Andrew Smye, Nelson Boniface, William Craddock, and an anonymous reviewer for their keen and constructive reviews, which served to greatly improve the manuscript. Any use of trade, firm, or product names is for descriptive purposes only and does not imply endorsement by the U.S. Government.

Author contributions Apen, Rudnick, Cottle, and Blondes conceived project ideas; Apen conducted analyses with assistance from Kylander-Clark, Seward, and Piccoli; Apen and Rudnick wrote main text with input from all authors.

Funding NSF Grants EAR-0337255 awarded to R. L. Rudnick and EAR-1650260 awarded to R. L. Rudnick and J. M. Cottle, as well as a Grant to R. L. Rudnick from the National Geographic Society (7836-05). F. E. Apen was supported by an NSF graduate fellowship.

Code availability Not applicable

Compliance with ethical standards

Conflict of interest Not applicable

Availability of data and material Not applicable.

References

- Ague JJ, Baxter EF (2007) Brief thermal pulses during mountain building recorded by Sr diffusion in apatite and multicomponent diffusion in garnet. Earth Planet Sci Lett 261:500–516. https://doi.org/10.1016/j.epsl.2007.07.017
- Appel P, Möller A, Schenk V (1998) High-pressure granulite facies metamorphism in the Pan-African belt of eastern Tanzania: P-T-t evidence against granulite formation by continent collision. J Metamorph Geol 16:491–509. https://doi.org/10.111 1/j.1525-1314.1998.00150.x
- Aulbach S, Rudnick RL, McDonough WF (2008) Li-Sr-Nd isotope signatures of the plume and cratonic lithospheric mantle beneath the margin of the rifted Tanzanian craton (Labait). Contrib Mineral Petrol 155:79–92. https://doi.org/10.1007/s00410-007-0226-4
- Aulbach S, Rudnick RL, McDonough WF (2011) Evolution of the lithospheric mantle beneath the East African Rift in Tanzania and its potential signatures in rift magmas. Spec Pap Geol Soc Am 478:105–125. https://doi.org/10.1130/2011.2478(06)
- Bellucci JJ, McDonough WF, Rudnick RL (2011) Thermal history and origin of the Tanzanian Craton from Pb isotope thermochronology of feldspars from lower crustal xenoliths. Earth Planet Sci Lett 301:493–501. https://doi.org/10.1016/j.epsl.2010.11.031
- Bingen B, Demaiffe D, Hertogen J (1996) Redistribution of rare earth elements, thorium, and uranium over accessory minerals in the course of amphibolite to granulite facies metamorphism: The role of apatite and monazite in orthogneisses from

- southwestern Norway. Geochim Cosmochim Acta 60:1341–1354. https://doi.org/10.1016/0016-7037(96)00006-3
- Blackburn T, Bowring SA, Schoene B et al (2011) U-Pb thermochronology: creating a temporal record of lithosphere thermal evolution. Contrib to Mineral Petrol 162:479–500. https://doi.org/10.1007/s00410-011-0607-6
- Bohlen SR, Mezger K (1989) Origin of granulite terranes and the formation of the lowermost continental crust. Science 244:326–329. https://doi.org/10.1126/science.244.4902.326
- Bonamici CE, Fanning CM, Kozdon R et al (2015) Combined oxygen-isotope and U-Pb zoning studies of titanite: new criteria for age preservation. Chem Geol 398:70-84. https://doi.org/10.1016/j.chemgeo.2015.02.002
- Burton KW, Schiano P, Birck J-L et al (2000) The distribution and behaviour of rhenium and osmium amongst mantle minerals and the age of the lithospheric mantle beneath Tanzania. Earth Planet Sci Lett 183:93–106. https://doi.org/10.1016/S0012-821X(00)00259-4
- Canil D, O'Neill HSC, Pearson DG et al (1994) Ferric iron in peridotites and mantle oxidation states. Earth Planet Sci Lett 123:205–220. https://doi.org/10.1016/0012-821X(94)90268-2
- Cherniak DJ (1993) Lead diffusion in titanite and preliminary results on the effects of radiation damage on Pb transport. Chem Geol 110:177–194. https://doi.org/10.1016/0009-2541(93)90253-F
- Cherniak DJ (1995) Sr and Nd diffusion in titanite. Chem Geol 125:219–232. https://doi.org/10.1016/0009-2541(95)00074-V
- Cherniak DJ (2000) Pb diffusion in rutile. Contrib Mineral Petrol 139:198–207. https://doi.org/10.1007/PL00007671
- Cherniak DJ (2006) Zr diffusion in titanite. Contrib Mineral Petrol 152:639–647. https://doi.org/10.1007/s00410-006-0133-0
- Cherniak DJ (2010) Diffusion in accessory minerals: zircon, titanite, apatite, monazite and xenotime. Rev Mineral Geochem 72:827–869. https://doi.org/10.2138/rmg.2010.72.18
- Cherniak DJ, Lanford WA, Ryerson FJ (1991) Lead diffusion in apatite and zircon using ion implantation and Rutherford Backscattering techniques. Geochim Cosmochim Acta 55:1663–1673. https://doi.org/10.1016/0016-7037(91)90137-T
- Chesley JT, Rudnick RL, Lee CT (1999) Re-Os systematics of mantle xenoliths from the East African Rift: age, structure, and history of the Tanzanian craton. Geochim Cosmochim Acta 63:1203–1217. https://doi.org/10.1016/S0016-7037(99)00004
- Chin EJ (2018) Deep crustal cumulates reflect patterns of continental rift volcanism beneath Tanzania. Contrib Mineral Petrol 173:1–22. https://doi.org/10.1007/s00410-018-1512-z
- Clark C, Taylor RJM, Johnson TE et al (2019) Testing the fidelity of thermometers at ultrahigh temperatures. J Metamorph Geol 37:917–934. https://doi.org/10.1111/jmg.12486
- Cochrane R, Spikings RA, Chew D et al (2014) High temperature (>350 °C) thermochronology and mechanisms of Pb loss in apatite. Geochim Cosmochim Acta 127:39–56. https://doi.org/10.1016/j.gca.2013.11.028
- Cohen RS, O'Nions RK, Dawson JB (1984) Isotope geochemistry of xenoliths from East Africa: implications for development of mantle reservoirs and their interaction. Earth Planet Sci Lett 68:209–220. https://doi.org/10.1016/0012-821X(84)90153-5
- Coolen JJMM, Priem HN, Verdurmen EAT, Verschure R (1982) Possible zircon U–Pb evidence for Pan-African granulite-facies metamorphism in the Mozambique belt of southern Tanzania. Precambrian Res 17:31–40. https://doi.org/10.1016/0301-9268(82)90152-8
- Corfu F, Hanchar JM, Hoskin PWO, Kinny PD (2003) Atlas of zircon textures. Rev Mineral Geochem 53:469–500. https://doi.org/10.2113/0530469
- Crank J (1975) The mathematics of diffusion, 2nd edn. Oxford Science Publications, Oxford



- Cutten H, Johnson SP, De WB (2006) Protolith ages and timing of metasomatism related to the formation of whiteschists at Mautia Hill, Tanzania: implications for the Assembly of Gondwana. J Geol 114:683–698. https://doi.org/10.1086/507614
- Davis WJ (1997) U-Pb zircon and rutile ages from granulite xenoliths in the Slave province: evidence for mafic magmatism in the lower crust coincident with Proterozoic dike swarms. Geology 25:343-346. https://doi.org/10.1130/0091-7613(1997)025<0343:UPZARA>2.3.CO;2
- Davis WJ, Canil D, MacKenzie JM, Carbno GB (2003) Petrology and U-Pb geochronology of lower crustal xenoliths and the development of a craton, Slave Province, Canada. Lithos 71:541–573. https://doi.org/10.1016/S0024-4937(03)00130-0
- Dawson JB (1992) Neogene tectonics and volcanicity in the North Tanzania sector of the Gregory Rift Valley: contrasts with the Kenya sector. Tectonophysics 204:81. https://doi.org/10.1016/0040-1951(92)90271-7
- Dawson JB (2002) Metasomatism and partial melting in upper-mantle Peridotite Xenoliths from the Lashaine Volcano, Northern Tanzania. J Petrol 43:1749–1777. https://doi.org/10.1093/petro logy/43.9.1749
- Dawson JB, Smith JV (1988) Metasomatised and veined upper-mantle xenoliths from Pello Hill, Tanzania: evidence for anomalously-light mantle beneath the Tanzanian sector of the East African Rift Valley. Contrib Mineral Petrol 100:510–527. https://doi.org/10.1007/BF00371380
- Dawson JB, Smith JV (1992) Olivine-mica pyroxenite xenoliths from northern Tanzania: metasomatic products of upper-mantle peridotite. J Volcanol Geotherm Res 50:131–142. https://doi. org/10.1016/0377-0273(92)90041-B
- Dawson JB, Powell DG, Reid AM (1970) Ultrabasic xenoliths and lava from the lashaine Volcano, Northern Tanzania. J Petrol 11:519–548. https://doi.org/10.1093/petrology/11.3.519
- Dodson MH (1986) Closure profiles in cooling systems. Mater Sci Forum 7:145–154. https://doi.org/10.4028/www.scientific.net/ MSF.7.145
- Ebinger CJ (1989) Tectonic development of the western branch of the East African rift system. Geol Soc Am Bull 101:885–903. https://doi.org/10.1130/0016-7606(1989)101<0885:TDOTW B>2.3.CO;2
- Ernst WG, Liu J (1998) Experimental phase-equilibrium study of Al- and Ti-contents of calcic amphibole in MORB; a semi-quantitative thermobarometer. Am Mineral 83:952–969. https://doi.org/10.2138/am-1998-9-1004
- Ewing TA, Hermann J, Rubatto D (2013) The robustness of the Zr-in-rutile and Ti-in-zircon thermometers during high-temperature metamorphism (Ivrea-Verbano Zone, northern Italy). Contrib to Mineral Petrol 165:757–779. https://doi.org/10.1007/s00410-012-0834-5
- Ferry JM, Watson EB (2007) New thermodynamic models and revised calibrations for the Ti-in-zircon and Zr-in-rutile thermometers. Contrib Mineral Petrol 154:429–437. https://doi.org/10.1007/s00410-007-0201-0
- Foster A, Ebinger C, Mbede E, Rex D (1997) Tectonic development of the northern Tanzanian sector of the East African Rift System. J Geol Soc London 154:689–700. https://doi.org/10.1144/gsjgs.154.4.0689
- Fritz H, Tenczer V, Hauzenberger CA, et al (2005) Central Tanzanian tectonic map: a step forward to decipher proterozoic structural events in the East African Orogen. Tectonics 24. https://doi.org/10.1029/2005TC001796
- Fritz H, Tenczer V, Hauzenberger C et al (2009) Hot granulite nappes-tectonic styles and thermal evolution of the Proterozoic granulite belts in East Africa. Tectonophysics 477:160–173. https://doi.org/10.1016/j.tecto.2009.01.021

- Fritz H, Abdelsalam M, Ali KA et al (2013) Orogen styles in the East African Orogen: a review of the Neoproterozoic to Cambrian tectonic evolution. J Afr Earth Sci 86:65–106. https://doi.org/10.1016/j.jafrearsci.2013.06.004
- Frost BR, Chamberlain KR, Schumacher JC (2001) Sphene (titanite): phase relations and role as a geochronometer. Chem Geol 172:131–148. https://doi.org/10.1016/S0009-2541(00)00240-0
- Furlong KP, Chapman DS (2013) Heat flow, heat generation, and the thermal state of the lithosphere. Annu Rev Earth Planet Sci 41:385–410. https://doi.org/10.1146/annurev.earth.03120 8 100051
- Garber JM, Hacker BR, Kylander-Clark ARC et al (2017) Controls on trace element uptake in metamorphic titanite: implications for petrochronology. J Petrol 58:1031–1057. https://doi.org/10.1093/petrology/egx046
- Harlov DE, Wirth R, Förster HJ (2005) An experimental study of dissolution-reprecipitation in fluorapatite: fluid infiltration and the formation of monazite. Contrib Mineral Petrol 150:268–286. https://doi.org/10.1007/s00410-005-0017-8
- Hasterok D, Chapman DS (2011) Heat production and geotherms for the continental lithosphere. Earth Planet Sci Lett 307:59–70. https://doi.org/10.1016/j.epsl.2011.04.034
- Hauzenberger CA, Sommer H, Fritz H et al (2007) SHRIMP U-Pb zircon and Sm-Nd garnet ages from the granulite-facies basement of SE Kenya: evidence for Neoproterozoic polycyclic assembly of the Mozambique Belt. J Geol Soc London 164:189–201. https://doi.org/10.1144/0016-76492005-081
- Hayden LA, Watson EB, Wark DA (2008) A thermobarometer for sphene (titanite). Contrib to Mineral Petrol 155:529–540. https://doi.org/10.1007/s00410-007-0256-y
- Henrichs IA, Chew DM, O'Sullivan GJ et al (2019) Trace Element (Mn-Sr-Y-Th-REE) and U-Pb isotope systematics of metapelitic apatite during progressive greenschist- to amphibolite-facies Barrovian metamorphism. Geochem Geophys Geosyst 20:4103–4129. https://doi.org/10.1029/2019GC008359
- Hinton RW, Upton BGJ (1991) The chemistry of zircon: variations within and between large crystals from syenite and alkali basalt xenoliths. Geochim Cosmochim Acta 55:3287–3302. https://doi.org/10.1016/0016-7037(91)90489-R
- Holder RM, Hacker BR (2019) Fluid-driven resetting of titanite following ultrahigh-temperature metamorphism in southern Madagascar. Chem Geol 504:38–52. https://doi.org/10.1016/j.chemgeo.2018.11.017
- Holder RM, Hacker BR, Seward GGE, Kylander-Clark ARC (2019) Interpreting titanite U-Pb dates and Zr thermobarometry in highgrade rocks: empirical constraints on elemental diffusivities of Pb, Al, Fe, Zr, Nb, and Ce. Contrib Mineral Petrol 174. https:// doi.org/10.1007/s00410-019-1578-2
- Jaupart C, Mareschal JC (2014) Constraints on crustal heat production from heat flow data, 2nd edn. Elsevier Ltd., The Netherlands
- Johnson SP, Cutten HNC, Muhongo S, De Waele B (2003) Neoar-chaean magmatism and metamorphism of the western granulites in the central domain of the Mozambique belt, Tanzania: U-Pb shrimp geochronology and PT estimates. Tectonophysics 375:125–145. https://doi.org/10.1016/j.tecto.2003.06.003
- Jones AP, Smith JV, Dawson JB, Hansen EC (1983) Metamorphism, partial melting, and K-metasomatism of garnet-scapolite-kyanite granulite xenoliths from Lashaine, Tanzania. J Geol 91:143–165. https://doi.org/10.1086/628753
- Julià J, Ammon CJ, Nyblade AA (2005) Evidence for mafic lower crust in Tanzania, East Africa, from joint inversion of receiver functions and Rayleigh wave dispersion velocities. Geophys J Int 162:555–569. https://doi.org/10.1111/j.1365-246X.2005.02685.x
- Kelsey DE, Powell R (2011) Progress in linking accessory mineral growth and breakdown to major mineral evolution in metamorphic rocks: a thermodynamic approach in the



- Na₂O-CaO-K₂O-FeO-MgO-Al₂O₃-SiO₂-H₂O-TiO₂-ZrO₂ system. J Metamorph Geol 29:151–166. https://doi.org/10.1111/j.1525-1314.2010.00910.x
- Kohn MJ (2017) Titanite petrochronology. Rev Mineral Geochemistry 83:419–441. https://doi.org/10.2138/rmg.2017.83.13
- Kohn MJ, Kelly NM (2017) Petrology and geochronology of metamorphic zircon. Microstruct Geochronol Planet Rec Down to Atom Scale 35–61. https://doi.org/10.1002/9781119227250. ch2
- Kohn MJ, Penniston-Dorland SC, Ferreira JCS (2016) Implications of near-rim compositional zoning in rutile for geothermometry, geospeedometry, and trace element equilibration. Contrib Mineral Petrol 171:78. https://doi.org/10.1007/s00410-016-1285-1
- Kooijman E, Mezger K, Berndt J (2010) Constraints on the U-Pb systematics of metamorphic rutile from in situ LA-ICP-MS analysis. Earth Planet Sci Lett 293:321–330. https://doi.org/10.1016/j.epsl.2010.02.047
- Kooijman E, Smit MA, Mezger K, Berndt J (2012) Trace element systematics in granulite facies rutile: Implications for Zr geother-mometry and provenance studies. J Metamorph Geol 30:397–412. https://doi.org/10.1111/j.1525-1314.2012.00972.x
- Kylander-Clark ARC, Hacker BR, Cottle JM (2013) Laser-ablation split-stream ICP petrochronology. Chem Geol 345:99–112. https://doi.org/10.1016/j.chemgeo.2013.02.019
- Le Gall B, Gernigon L, Rolet J et al (2004) Neogene-Holocene rift propagation in central Tanzania: morphostructural and aeromagnetic evidence from the Kilombero area. Bull Geol Soc Am 116:490–510. https://doi.org/10.1130/B25202.1
- Le Gall B, Nonnotte P, Rolet J et al (2008) Rift propagation at craton margin. distribution of faulting and volcanism in the North Tanzanian Divergence (East Africa) during Neogene times. Tectonophysics 448:1–19. https://doi.org/10.1016/j.tecto.2007.11.005
- Le Goff E, Deschamps Y, Guerrot C (2010) Tectonic implications of new single zircon Pb–Pb evaporation data in the Lossogonoi and Longido ruby-districts, Mozambican metamorphic Belt of northeastern Tanzania. Comptes Rendus Geosci 342:36–45. https://doi.org/10.1016/j.crte.2009.10.003
- Lee CTA, Rudnick RL (1999) Compositionally stratified cratonic lithosphere: petrology and geochemistry of peridotite xenoliths the Labait volcano, Tanzania. In: Proc 7th Internatl Kimberl Conf, Vol I Dawson Vol 503–521
- Maboko MAH (1997) P–T conditions of metamorphism in the Wami River granulite complex, central coastal Tanzania: implications for Pan-African geotectonics in the Mozambique Belt of eastern Africa. J Afr Earth Sci 24:51–64. https://doi.org/10.1016/S0899 -5362(97)00026-2
- Maboko MAH (2000) Nd and Sr isotopic investigation of the Archean-Proterozoic boundary in north eastern Tanzania: constraints on the nature of Neoproterozoic tectonism in the Mozambique Belt. Precambrian Res 102:87–98. https://doi.org/10.1016/S0301-9268(00)00060-7
- Maboko MAH (2001) Dating post-metamorphic cooling of the Eastern Granulites in the Mozambique Belt of Northern Tanzania using the Garnet Sm-Nd method. Gondwana Res 4:329–336. https://doi.org/10.1016/S1342-937X(05)70333-6
- Maboko MAH, Nakamura E (2002) Isotopic dating of Neoproterozoic crustal growth in the Usambara Mountains of northeastern Tanzania: evidence for coeval crust formation in the Mozambique Belt and the Arabian–Nubian Shield. Precambrian Res 113:227–242. https://doi.org/10.1016/S0301-9268(01)00213-3
- Maboko MAH, McDougall I, Zeitler PK (1989) Dating late Pan-African cooling in the Uluguru granulite complex of Eastern Tanzania using the 40Ar–39Ar technique. J Afr Earth Sci (and Middle East) 9:159–167. https://doi.org/10.1016/0899-5362(89)90017-1
- Maboko M, Pedersen R, Manya S, et al (2006) The origin of late archaean granitoids in the Sukumaland greenstone belt of

- Northern Tanzania: geochemical and isotopic constraints. Tanzania J Sci 32. https://doi.org/10.4314/tjs.v32i1.18431
- Manning CF, Bohlen SR (1991) The reaction titanite+kyanite=anor thite+rutile and titanite-rutile barometry in eclogites. Contrib Mineral Petrol 109:1–9. https://doi.org/10.1007/BF00687196
- Mansur AT, Manya S, Timpa S, Rudnick RL (2014) Granulite-facies xenoliths in rift basalts of Northern Tanzania: age, composition and origin of Archean Lower Crust. J Petrol 55:1243–1286. https://doi.org/10.1093/petrology/egu024
- Manya S, Maboko MAH (2003) Dating basaltic volcanism in the Neoarchaean Sukumaland Greenstone Belt of the Tanzania Craton using the Sm-Nd method: implications for the geological evolution of the Tanzania Craton. Precambrian Res 121:35–45. https://doi.org/10.1016/S0301-9268(02)00195-X
- Manya S, Kobayashi K, Maboko MAH, Nakamura E (2006) Ion microprobe zircon U–Pb dating of the late Archaean metavolcanics and associated granites of the Musoma-Mara Greenstone Belt, Northeast Tanzania: Implications for the geological evolution of the Tanzania Craton. J Afr Earth Sci 45:355–366. https://doi. org/10.1016/j.jafrearsci.2006.03.004
- Marsh JH, Smye AJ (2017) U-Pb systematics and trace element characteristics in titanite from a high-pressure mafic granulite. Chem Geol 466:403–416. https://doi.org/10.1016/j.chemgeo.2017.06.029
- McDonough WF, Sun S (1995) The composition of the earth. Chem Geol 120:223–253. https://doi.org/10.1016/0009-2541(94)00140
- Meert J (1995) Paleomagnetic investigation of the Neoproterozoic Gagwe lavas and Mbozi complex, Tanzania and the assembly of Gondwana. Precambrian Res 74:225–244. https://doi.org/10.1016/0301-9268(95)00012-T
- Meert JG (2003) A synopsis of events related to the assembly of eastern Gondwana. Tectonophysics 362:1–40. https://doi.org/10.1016/S0040-1951(02)00629-7
- Mole DR, Barnes SJ, Taylor RJM et al (2018) A relic of the Mozambique Ocean in south-east Tanzania. Precambrian Res 305:386–426. https://doi.org/10.1016/j.precamres.2017.10.009
- Möller A, Mezger K, Schenk V (1998) Crustal age domains and the evolution of the continental crust in the Mozambique Belt of Tanzania: combined Sm–Nd, Rb–Sr, and Pb–Pb isotopic evidence. J Petrol 39:749–783. https://doi.org/10.1093/petroj/39.4.749
- Möller A, Mezger K, Schenk V (2000) U–Pb dating of metamorphic minerals: Pan-African metamorphism and prolonged slow cooling of high pressure granulites in Tanzania, East Africa. Precambrian Res 104:123–146. https://doi.org/10.1016/S0301-9268(00)00086-3
- Mtabazi EG, Boniface N, Andresen A (2019) Geochronological characterization of a transition zone between the Mozambique Belt and Unango-Marrupa Complex in SE Tanzania. Precambrian Res 321:134–153. https://doi.org/10.1016/j.precamres.2018.11.017
- Muhongo S, Tuisku P (1996) Pan-African high pressure isobaric cooling: evidence from the mineralogy and thermobarometry of the granulite-facies rocks from the Uluguru Mountains, eastern Tanzania. J Afr Earth Sci 23:443–463. https://doi.org/10.1016/S0899-5362(97)00012-2
- Muhongo S, Tuisku P, Mtoni Y (1999) Pan-African pressure-temperature evolution of the Merelani area in the Mozambique Belt in northeast Tanzania. J Afr Earth Sci 29:353–365. https://doi.org/10.1016/S0899-5362(99)00102-5
- Nyblade AA (1997) Heat flow across the East African Plateau. Geophys Res Lett 24:2083–2086. https://doi.org/10.1029/97GL0
- Nyblade AA, Brazier RA (2002) Precambrian lithospheric controls on the development of the East African rift system. Geology 30:755–758. https://doi.org/10.1130/0091-7613(2002)030<0755:PLCOT D>2.0.CO;2



- Nyblade AA, Pollack HN, Jones DL et al (1990) Terrestrial heat flow in east and southern Africa. J Geophys Res 95:17371. https://doi.org/10.1029/JB095iB11p17371
- Pape J, Mezger K, Robyr M (2016) A systematic evaluation of the Zr-in-rutile thermometer in ultra-high temperature (UHT) rocks. Contrib Mineral Petrol 171:1–20. https://doi.org/10.1007/s0041 0-016-1254-8
- Paul AN, Spikings RA, Chew D, Daly JS (2019) The effect of intracrystal uranium zonation on apatite U–Pb thermochronology: a combined ID-TIMS and LA-MC-ICP-MS study. Geochim Cosmochim Acta 251:15–35. https://doi.org/10.1016/j. gca.2019.02.013
- Pollack HN, Chapman DS (1977) Mantle heat flow. Earth Planet Sci Lett 34:174–184. https://doi.org/10.1016/0012-821X(77)90002-4
- Ridley WI, Dawson JB (1975) Lithophile trace element data bearing on the origin of peridotite xenoliths, ankaramite and carbonatite from Lashaine volcano. In: Tanzania N (ed) Physics and chemistry of the earth. Elsevier, The Netherlands, pp 559–569
- Ritsema J, Nyblade AA, Owens TJ et al (1998) Upper mantle seismic velocity structure beneath Tanzania, east Africa: implications for the stability of cratonic lithosphere. J Geophys Res Solid Earth 103:21201–21213. https://doi.org/10.1029/98jb01274
- Rubatto D (2002) Zircon trace element geochemistry: partitioning with garnet and the link between U-Pb ages and metamorphism. Chem Geol 184:123–138. https://doi.org/10.1016/S0009-2541(01)00355-2
- Rudnick RL, McDonough WF, Chappell BC (1993) Carbonatite metasomatism in the northern Tanzanian mantle. Earth Planet Sci Lett 114:463–475
- Rudnick RL, McDonough WF, Orpin A (1994) Northern Tanzanian peridotite xenoliths: a comparison with Kaapvaal peridotites and inferences on metasomatic interactions. In: Meyer HOA, Leonardos OH (eds) Proceedings of the Vth international kimberlite conference, vol 1, pp 336–352
- Rudnick RL, McDonough WF, O'Connell RJ (1998) Thermal structure, thickness and composition of continental lithosphere. Chem Geol 145:395–411. https://doi.org/10.1016/S0009-2541(97)00151-4
- Sanislav IV, Wormald RJ, Dirks PHGM et al (2014) Zircon U–Pb ages and Lu-Hf isotope systematics from late-tectonic granites, Geita Greenstone Belt: implications for crustal growth of the Tanzania Craton. Precambrian Res 242:187–204. https://doi.org/10.1016/j.precamres.2013.12.026
- Sanislav IV, Dirks PHGM, Blenkinsop T, Kolling SL (2018) The tectonic history of a crustal-scale shear zone in the Tanzania Craton from the Geita Greenstone Belt, NW-Tanzania Craton. Precambrian Res 310:1–16. https://doi.org/10.1016/j.precamres.2018.02.025
- Schmitz MD, Bowring SA (2003a) Ultrahigh-temperature metamorphism in the lower crust during Neoarchean Ventersdorp rifting and magmatism, Kaapvaal craton, southern Africa. Bull Geol Soc Am 115:533–548. https://doi.org/10.1130/0016-7606(2003)115<0533:UMITLC>2.0.CO;2
- Schmitz MD, Bowring SA (2003b) Constraints on the thermal evolution of continental lithosphere from U–Pb accessory mineral thermochronometry of lower crustal xenoliths, southern Africa. Contrib Mineral Petrol 144:592–618. https://doi.org/10.1007/s00410-002-0419-9
- Smye AJ, Stockli DF (2014) Rutile U-Pb age depth profiling: a continuous record of lithospheric thermal evolution. Earth Planet Sci Lett 408:171-182. https://doi.org/10.1016/j.epsl.2014.10.013
- Smye AJ, Marsh JH, Vermeesch P et al (2018) Applications and limitations of U-Pb thermochronology to middle and lower crustal thermal histories. Chem Geol 494:1-18. https://doi.org/10.1016/j.chemgeo.2018.07.003
- Sommer H, Kröner A, Hauzenberger C et al (2003) Metamorphic petrology and zircon geochronology of high-grade rocks from

- the central Mozambique Belt of Tanzania: crustal recycling of Archean and Palaeoproterozoic material during the Pan-African orogeny. J Metamorph Geol 21:915–934. https://doi.org/10.1111/j.1525-1314.2003.00491.x
- Sommer H, Kröner A, Hauzenberger C, Muhongo S (2005) Reworking of archaean and Palaeoproterozoic crust in the Mozambique belt of central Tanzania as documented by SHRIMP zircon geochronology. J Afr Earth Sci 43:447–463. https://doi.org/10.1016/j.jafrearsci.2005.09.005
- Sommer H, Hauzenberger C, Kröner A, Muhongo S (2008) Isothermal decompression history in the "Western Granulite" terrain, central Tanzania: evidence from reaction textures and trapped fluids in metapelites. J African Earth Sci 51:123–144. https://doi.org/10.1016/j.jafrearsci.2008.01.003
- Spear FS, Pyle JM (2002) Apatite, monazite, and xenotime in metamorphic rocks. Rev Mineral Geochem 48:293–335. https://doi.org/10.2138/rmg.2002.48.7
- Spencer KJ, Hacker BR, Kylander-Clark ARC et al (2013) Campaignstyle titanite U-Pb dating by laser-ablation ICP: implications for crustal flow, phase transformations and titanite closure. Chem Geol 341:84–101. https://doi.org/10.1016/j.chemgeo.2012.11.012
- Stearns MA, Cottle JM, Hacker BR, Kylander-Clark ARC (2016) Extracting thermal histories from the near-rim zoning in titanite using coupled U–Pb and trace element depth profiles by singleshot laser-ablation split stream (SS-LASS) ICP–MS. Chem Geol 422:13–24. https://doi.org/10.1016/j.chemgeo.2015.12.011
- Stern RJ (1994) Arc assembly and continental collision in the neoproterozoic East African Orogen: implications for the consolidation of Gondwanaland. Annu Rev Earth Planet Sci 22:319–351. https://doi.org/10.1146/annurev.ea.22.050194.001535
- Taylor RJM, Harley SL, Hinton RW et al (2015) Experimental determination of REE partition coefficients between zircon, garnet and melt: a key to understanding high-T crustal processes. J Metamorph Geol 33:231–248. https://doi.org/10.1111/jmg.12118
- Taylor-Jones K, Powell R (2015) Interpreting zirconium-in-rutile thermometric results. J Metamorph Geol 33:115–122. https://doi.org/10.1111/jmg.12109
- Tenczer V, Hauzenberger CA, Fritz H et al (2006) Anorthosites in the Eastern Granulites of Tanzania-New SIMS zircon U-Pb age data, petrography and geochemistry. Precambrian Res 148:85–114. https://doi.org/10.1016/j.precamres.2006.03.004
- Tenczer V, Hauzenberger C, Fritz H et al (2013) Crustal age domains and metamorphic reworking of the deep crust in Northern-Central Tanzania: a U/Pb zircon and monazite age study. Mineral Petrol 107:679–707. https://doi.org/10.1007/s00710-012-0210-1
- Thomas RJ, Spencer C, Bushi AM et al (2016) Geochronology of the central Tanzania Craton and its southern and eastern orogenic margins. Precambrian Res 277:47–67. https://doi.org/10.1016/j.precamres.2016.02.008
- Tomkins HS, Powell R, Ellis DJ (2007) The pressure dependence of the zirconium-in-rutile thermometer. J Metamorph Geol 25:703–713. https://doi.org/10.1111/j.1525-1314.2007.00724.x
- Trail D, Bruce Watson E, Tailby ND (2012) Ce and Eu anomalies in zircon as proxies for the oxidation state of magmas. Geochim Cosmochim Acta 97:70–87. https://doi.org/10.1016/j.gca.2012.08.032
- Vauchez A, Dineur F, Rudnick R (2005) Microstructure, texture and seismic anisotropy of the lithospheric mantle above a mantle plume: insights from the Labait volcano xenoliths (Tanzania). Earth Planet Sci Lett 232:295–314. https://doi.org/10.1016/j.epsl.2005.01.024
- Walters JB, Kohn MJ (2017) Protracted thrusting followed by late rapid cooling of the Greater Himalayan Sequence, Annapurna Himalaya, Central Nepal: insights from titanite petrochronology. J Metamorph Geol 35:897–917. https://doi.org/10.1111/jmg.12260



- Weeraratne DS, Forsyth DW, Fischer KM, Nyblade AA (2003) Evidence for an upper mantle plume beneath the Tanzanian craton from Rayleigh wave tomography. J Geophys Res Solid Earth 108: https://doi.org/10.1029/2002jb002273
- Whitehouse MJ, Platt JP (2003) Dating high-grade metamorphism constraints from rare-earth elements in zircon and garnet. Contrib Mineral Petrol 145:61-74. https://doi.org/10.1007/s0041 0-002-0432-z
- Xu Y, Tang W, Hui H et al (2019) Reconciling the discrepancy between the dehydration rates in mantle olivine and pyroxene during xenolith emplacement. Geochim Cosmochim Acta 267:179–195. https://doi.org/10.1016/j.gca.2019.09.023
- Yakymchuk C, Brown M (2014) Behaviour of zircon and monazite during crustal melting. J Geol Soc London 171:465-479. https ://doi.org/10.1144/jgs2013-115

- Zack T, Kooijman E (2018) Petrology and geochronology of rutile. Petrochronol Methods Appl 83:443-467. https://doi.org/10.2138/ rmg.2017.83.14
- Zack T, Moraes R, Kronz A (2004) Temperature dependence of Zr in rutile: empirical calibration of a rutile thermometer. Contrib Mineral Petrol 148:471–488. https://doi.org/10.1007/s0041 0-004-0617-8

Publisher's Note Springer Nature remains neutral with regard to jurisdictional claims in published maps and institutional affiliations.

